Supporting Information
An Autonomous Molecular Bioluminescent Reporter (AMBER) for Voltage Imaging in Freely Moving Animals

Prasanna Srinivasan, Nicole M Griffin, Dhananjay Thakur, Pradeep Joshi,
Alex Nguyen-Le, Sean McCotter, Akshar Jain, Mitra Saeidi, Prajakta Kulkarni,
Jaclyn T. Eisdorfer, Joel Rothman, Craig Montell, Luke Theogarajan

1 Materials and Methods

1.1 Safety Statement

All experiments were conducted in accordance to the biosafety protocols approved by the UCSB Environmental Health and Safety following the reagent manufacturer's guidelines. No vertebrate animals were used in our experiments.

1.2 Molecular Cloning of Engineered Protein Constructs

We used two plasmids - pCMV$_{\text{lux}}$ and pcDNA3.1-VSFP2.1 to create plasmids that encode different engineered protein constructs for expression in mammalian cells. pCMV$_{\text{lux}}$ purchased from the 490 Biotech encodes for the mammalian codon-optimized lux operon proteins. pcDNA3.1-VSFP2.1 was a gift from Thomas Knopfel laboratory (Addgene plasmid# 1255; http://n2t.net/addgene:16255; RRID: Addgene_16255).

We applied a structure-function relationship to assess the functional equivalence of *P. luminescens* luxAB (pl-luxAB) and YPet fusion BRET pair for Cerulean/Citrine FRET pair in VSFP2.1. Both YPet and Citrine proteins, derived from eYFP [17, 29] are variants of GFP that fold into a characteristic beta-barrel structure. In contrast, pl-luxAB structure has not yet been solved although it shares a substantial amino acid sequence identity (93% and 76% positives for luxA and luxB domains) with *V. harveyi* luxAB (vh-luxAB). vh-luxAB halo enzyme is self-assembly of vh-luxA and vh-luxB domains, which has an inter-digitated TIM (Triosephosphate Isomerase) barrel structure[14, 1]. Self-assembly is achieved by hydrophobic interaction at the interface of luxA and luxB domains that directly influence the FMN binding pocket geometry. A fusion of vh-luxA and vh-luxB domains with a polypeptide linker can catalyze bioluminescent light reaction albeit with varied activity depending on the linker length [30]. We, therefore, hypothesized that replacing the FRET pair of VSFP2.1 with the luxAB-YPet BRET pair is a good starting point for optimizing light reaction sites.

We used the structural framework of VSFP2.1 [10] for designing the first generation AMBER. Our cloning strategy involves the following three steps; (i) base pair mutational changes for creating compatible restriction sites, (ii) synthesis of double-stranded insert fragments either by restriction endonuclease or Polymerase Chain Reaction (PCR using NEB Phusion-HF DNA polymerase; Catalog# M0530L) amplification of the cDNA with suitable primers and (iii) Fusion of the vector backbone and insert by ligation. We described the molecular biology approaches to sub-clone the cDNAs of various engineered constructs in mammalian and C.*elegans* expression vectors. We used shuttle vectors that allow genetic manipulation in bacteria and protein expression in the host cells. High fidelity restriction enzymes (HF versions, New England Biolabs) were used for overnight restriction digestion reactions to fully cut the DNA strands at the specific sites. Ligations were performed either with T4 DNA ligase (Catalog# M0202S; New England Biolabs inc.) or using in-fusion premix (Catalog# 639649; TaKaRa Bio Inc.) following the manufacturer's protocol. We used Stellar competent cells (Catalog# 636766; TaKaRa Bio Inc.) for the transformation of the ligation products before plating them onto LB agar plates with appropriate antibiotic selection.

We posited that replacement of the Cerulean domain of VSFP2.1 with a mammalian codon-optimized synthetic sequence of bacterial luciferase, enhanced luxAB [7] (henceforth called as 'eluxAB') will provide a baseline configuration for enhancing the biophotonic emission. We therefore modified the Citrine in VSFP2.1 to YPet, a bright variant of eYFP whose absorption spectrum substantially overlap with a broad luxAB emission spectrum. Fused luxAB retains its enzymatic activity [30]; therefore, we created a fusion linker between eluxA and eluxB in all the engineered probes. Implementing these changes to the pcDNA3.1-VSFP2.1 results in a plasmid that codes for the VE-Y protein. The remaining components of lux operon genes, *luxCDE-FRP* was kept intact in the $\mathrm{pCMV}_{\mathrm{lux}}$ backbone allowing polycistronic co-expression of luxCDE complex and FRP. Table S1 lists all the relevant biochemical reactions performed to create plasmids that allowed expressing all the engineered probes and their respective light producing substrates.

1.2.1 *VE-Y*

We began with replacing the Cerulean domain in pcDNA3.1-VSFP2.1 with the luxAB domain of $\mathrm{pCMV}_{\mathrm{lux}}$. This facilitated constructing plasmids that encode other candidates. The *Cerulean* sequence was flanked with NotI (1671) and BamHI (2374) sites. While the NotI site was unique, there were two BamHI sites (2374 and 3120) within the cDNA. To create a unique restriction site flanking the *Cerulean* sequence, the BamHI site at 3120 was mutated so that the open reading frame codes for the same amino acid using an alternative codon (a3122c). Unlike the *Cerulean* sequence in pcDNA3.1-VSFP2.1, there were no flanking restriction sites for the *luxAB* sequence in $\mathrm{pCMV}_{\mathrm{lux}}$. These sites were therefore created using site-directed mutagenesis substitution reactions. The requirement for minimal base pair changes (up to 4) allowed a NotI site to be placed 270bp upfront of *luxA* sequence thereby including a portion of *luxD* sequence in the chosen insert fragment (2300 bp). The *Cerulean* sequence was replaced with an insert obtained from the $\mathrm{pCMV}_{\mathrm{lux}}$ using restriction endonuclease (BamHI-HF and NotI-HF enzymes) and ligation (T4 DNA ligase) reactions. The additional 270bp that corresponds to a part of the *luxD* at the 5' end of the insert was removed by a deletion mutagenesis reaction to obtain *vsd-luxA-luxB-Citrine*. Functional mutations within the *luxA*, *luxB* and *Citrine* genes were introduced to create enhanced luciferase, *eluxA* and *eluxB* [7] and *YPet* respectively. Furthermore, $\mathrm{pCMV}_{\mathrm{lux}}$ contains a self-cleaving viral-2A genetic sequence between various genes of *lux* operon in the open reading frame to allow polycistronic expression of their respective proteins. We created mutants of viral-2A sequences reported previously [37] to abrogate self-cleavage between eluxA and eluxB proteins. The resulting modified cDNA, *VE-Y* encodes for a chimeric fusion polypeptide chain of Ciona voltage sensor (VSD), enhanced luciferase (eluxAB), and a bright fluorescent reporter (YPet).

1.2.2 *VY-E*

A BamHI site was introduced by substituting base pairs of EcorI at the 3' end of *VE-Y*. This enabled excising small (*YPet* gene) and large fragments with flanking BamHI sites by restriction digestion. Self-ligation of the large fragment created a plasmid that encodes the protein construct V-E. After interchanging the locations of BamHI and NotI sites in the *V-E* plasmid, the YPet fragment was re-introduced at the 3' end. This created a plasmid that codes the protein VY-E.

1.2.3 *luxCDE-FRP*

We excised out *luxA* and *luxB* gene fragments (3527-5746) from the $\mathrm{pCMV}_{\mathrm{lux}}$ plasmid using a deletion mutagenesis reaction. Nucleobases between the first base pair of luxA to the last base pair of P2A sequence was removed without disrupting the reading frame. This reaction results in a plasmid that encodes for polycistronic expression of luxCDE-FRP proteins.

1.2.4 *FV-E-Y*

We used a single BmtI site at the 5' end of *VE-Y* plasmid to introduce the FRP gene. The FRP gene fragment with flanking BmtI sites was created in the *luxCDE-FRP* using a substitution mutagenesis reaction. This reaction was followed by restriction endonuclease at the specific BmtI sites to obtain a small fragment (*FRP*) and a large fragment (*luxCDE*). *FRP* was then introduced at the BmtI site of *VE-Y* by restriction endonuclease and ligation reactions thereby creating a new plasmid *FRP-TAA-VSD-eluxAB-YPet*. The TAA stop codon at the 3' of FRP gene was mutated to a GGA (Glycine linker) to obtain the bright construct, *FV-E-Y*. Self ligation of the remaining large fragment resulted in the plasmid *luxCDE*, which encodes for the necessary substrate generating protein complexes.

1.2.5 *FV-Y-E*

We used the unique BmtI site at the 5' end of *VY-E* to introduce the *frp* gene. The *frp* gene fragment with flanking BmtI sites created earlier was introduced at the at the 5' BmtI site of *VY-E* by restriction endonuclease and ligation. These reactions were followed by substitution mutation of the TAA stop codon to GGA (Glycine linker) to create *FV-Y-E*. The *luxCDE* plasmid constructed earlier encodes for the necessary substrate-generating protein complexes.

1.2.6 *luxAB*

We fused the luxA and luxB genes in the pCMVlux by mutating the T2A element between them to abrogate the self-cleavage between these domains during translation. This change resulted in a plasmid that expresses soluble fusion protein luxAB.

1.2.7 *pCDNA3.1-rTRPV1*

The cDNA encoding for the recombinant fusion protein, MBP-8xHis-rTRPV1 (fusion of maltose binding protein with polyhistidine tag to rat TRPV1) cloned in an insect cell expression vector was a gift from David Julius laboratory, University of California, San Francisco. We sub-cloned the rTRPV1 domain into the mammalian expression vector pcDNA3.1(+) using in-fusion cloning approach. This involves restriction endonuclease of pcDNA3.1(+) at KpnI and EcoRI sites, PCR amplification of the rTRPV1 cDNA using primers with 15bp overlap at 3' and 5' ends of the vector, followed by a ligation using in-fusion enzyme mix (TaKaRa Bio Inc; Catalog# 639649). We performed temperature gradient PCR (primer melting temperature, T_m varying from 66-72°C) using 50ng template in a 20μL reaction volume. The primer sequences were optimized using Snapgene software (version 3.2.1) to achieve maximal PCR amplification. The PCR products were treated with DpnI enzyme (NEB, R0176S) to cut the methylated parent DNA template before agarose gel electrophoretic separation using TAE buffer (50X Tris-acetate-EDTA buffer, Catalog# FERB49; Fisher Scientific). The amplified DNA fragments in the gel were purified using a gel extraction kit (Catalog# 740609.50; TaKaRa Bio Inc) for the ligation.

1.2.8 *FV-E-Dark*

Plasmid encoding for the dark mutant of YPet (Gly65Thr, Gly67Ala) in FV-E-Y was obtained using commercially synthesized YPet genetic sequence with appropriate base-pair mutations. We purchased synthetic double-stranded DNA fragments (Genscript gene blocks) of mutated YPet with 15bp overlap at 3' and 5' ends of the vector flanking BamHI and EcoRI sites. The fluorescent YPet element was replaced with the mutated YPet fragment using restriction endonuclease of FV-E-Y and in-fusion reactions. The large fragment was obtained by electrophoretic separation of the digested products followed by extraction/purification using the gel extraction kit.

1.2.9 Subcloning AMBER constructs into *C. elegans* expression vectors

We sub-cloned *FV-E-Y* and *luxCDE* in *C. elegans* expression vectors targeting mechanosensory touch neurons and pharyngeal muscles. We used plasmids L3691 (Addgene plasmid# 1587) and L3790 (Addgene plasmid# 1596) obtained as a gift from Andy Fire laboratory. KpnI and EcoRI restriction sites of the L3691 vector were used to insert the cDNAs – *FV-E-Y* and *luxCDE* genes separately using infusion-cloning protocols. We optimized the primer sequences using the Snapgene software for sufficient PCR amplification of the cDNAs. PCR reactions were carried out using Phusion-HF DNA polymerase in a 20μL reaction volume containing 50ng of a template (either FV-E-Y or luxCDE). *FV-E-Y* required 3% DMSO (Dimethyl Sulfoxide) addition while *luxCDE* required an additional 0.5mM of $MgCl_2$. All PCR products were treated with DpnI enzyme overnight before electrophoretic separation in 2% agarose gel immersed in the 1X TAE buffer. The vector fragments were separately prepared by overnight restriction digestion followed by extraction and purification. The vector and the insert were fused using the infusion enzyme mix following the manufacturer's protocol. We denote the plasmids that express FV-E-Y and luxCDE proteins in *C. elegans* mechanosensory neurons as mec7-Btp ('Btp' represents Bright probe) and mec7-Bts ('Bts' represents Bright substrate) respectively

Plasmids that enable expression of FV-E-Y and luxCDE proteins in the pharyngeal muscles were constructed by replacing the mec-7 promoter sequence of mec7-Btp and mec7-Bts plasmids with a myo-2 promoter sequence from L3790. We performed restriction digestion of L3790 and mec7-Btp plasmids at SphI and ClaI sites and purified the vector and inserts after electrophoretic separation. We then fused the vector and insert using T4 DNA ligase enzyme following the manufacturer's protocol. The resultant plasmid obtained from this reaction is denoted as myo2-Btp. myo2-Bts was obtained using a synthetic myo-2 promoter gene (Genscript geneblocks) with flanking AscI and BamHI sites that replaces the corresponding nucleobases of mec7-Bts using infusion enzyme mix. The vector fragment with flanking AscI and BamHI sites was constructed by restriction digestion with AscI-HF (NEB; R0558S) and BamHI-HF enzymes followed by agarose gel electrophoretic separation and purification.

1.2.10 Molecular biology methods for subcloning the cDNAs into expression vectors

We performed all substitution, deletion, and insertion mutational changes using the QuickChange Lightning Site-Directed Mutagenesis kit (Agilent, Catalog# 210518). For implementing base pair changes at multiple locations simultaneously, we used the QuickChange Multi Site-Directed Mutagenesis kit (Agilent, Catalog# 200514). The mutational products were treated with DpnI enzyme to cut the parental template before transformation using XL10-Gold Ultracompetent cells (Agilent, Catalog# 200314). Five randomly picked colonies from an Ampicillin selection plate (10mL of polymerized LB-Agar containing 2% of LB Broth (Lennox; Sigma-Aldrich; Catalog# L7568-1KG), 1.5% of Bacto-Agar solidifying agent (BD Diagnostics, Supplier# 214010), and 1mg of Ampicillin sodium salt (Fisher Scientific, Catalog# BP1760-25)) were screened for every construct. The colonies were inoculated into 3mL LB media containing 1μL/mL of 100mg/mL Ampicllin stock and incubated for 12hrs inside a bacterial incubator (10L Benchmrk IncushakerTM; Benchmark Scientific, Item# H1010*) at 37^{o}C shaking at 225 rpm. Plasmid DNAs purified from the 3mL monoclonal culture using a DNA miniprep kit (GenCatch Plus Plasmid; Epoch Life Science; Catalog# 21-60250) were sequenced at either Genewiz or Berkeley Sequencing facilities to identify and confirm the positive clones. We used either universal primers or custom-made oligonucleotides to fully sequence the required regions of a plasmid. Plasmid DNAs of the positive clones that gave high-quality long reads (Q>45) were further sequenced to ensure a 100% match for the nucleobases of the coding region.

1.3 Expression of Engineered Proteins in HEK293 cells

We chemically transfected HEK293 cells (ATCC certified) with plasmid DNAs for live bioluminescent imaging. The cell culture protocol involves expanding a frozen stock of low passage cells (< 6) in a freshly prepared growth media containing 1X Dulbecco's Modified Eagle's Medium (high glucose DMEM containing 4.5g/L D-Glucose and L-Glutamine; ThermoFisher Scientific; Catalog# 11965-092), and 10% heat-inactivated Fetal Bovine Serum (Catalog# 10438026, ThermoFisher Scientific). Cells were grown on a 10 cm tissue culture dish (Catalog# 25-202; Genesee Scientific) inside an incubator (Forma Steri-Cult CO_2 Incubator; ThermoFisher Scientific; Catalog# 3307TS) containing 10% CO_2 maintained at 37^{o}C and 87%RH. We allowed the cells to proliferate at least for two passages splitting 1:10 every time after 80% confluence so that gene expression profiles are in the steady state. Each splitting involves dislodging the attached cells by Trypsin treatment (1mL of Trypsin-EDTA; Life Technologies; Catalog# 25200-056) for 1 min at 37^{o}C after a gentle wash with 1X PBS (ThermoFisher Scientific; Catalog# 10010023). We added 9mL of the growth media to stop the enzymatic activity of Trypsin and the dislodged cells were collected in suspension. The cell suspension was centrifuged (1000g for 5 min using HERMLE Z300) to retrieve the cells at the bottom of a 15mL tube (Catalog# 28-103; Genesee Scientific). The cells were washed with the growth media twice to minimize the amount of residual Trypsin if any in the collected cells.

We transfected $\approx 10^6$ cells with $\approx 1\mu g$ of DNA using the commercial Lipofectamine 2000 transfection reagent (ThermoFisher Scientific; Catalog# 11668027) in each batch. Engineered autonomous light production requires co-expression of both the probe molecule and its substrate producing complexes. We, therefore, used $\approx$ 500ng of probe and substrate plasmids for co-transfection. The protocol for preparing the transfection mix involves the preparation of two samples; one tube with $\approx$ 1μg DNA solubilized in 50μL of Opti-MEM and the other with 5μL Lipofectamine reagent mixed with 45μL of Opti-MEM. The contents of the tubes were then incubated at room temperature briefly for 2 min separately before mixing them and incubating for 30 minutes. The transfection mix was then directly mixed with $\approx 10^6$ cells (quantified using a hemacytometer, iN CYTO, Catalog# DHC-N01) suspended in 2mL of growth media and plated onto a 60 mm tissue culture dish (Corning Inc, Catalog# 430166). The dish was then placed inside the incubator for 7hrs. Meanwhile, a 12-well tissue culture plate (Catalog# 25-106; Genesee Scientific) containing 1% of poly-L-Lysine (PLL, Sigma Aldrich, Catalog# P8920-100ML) in PBS was incubated at room temperature inside a UV-sterilised hood. At 7hrs post-transfection, the media containing transfection mix was aspirated out. The attached transfected cells were gently washed with 1X PBS for dislodging by Trypsin treatment to plate them again onto PLL-treated wells (8 individual wells) of a 12-well plate at a seeding density of $\approx 10^5$ cells per well. The 12-well plate was maintained inside the incubator for at least 48 hours before using them for imaging assays. For plate reader assays, we replaced the media containing the transfection mix in a 60 mm dish with a fresh growth media after a gentle PBS wash at 7hrs post-transfection. We performed bioluminescent spectral recordings after 48 hours post-transfection. Before performing bioluminescent spectral recordings, the attached transfected cells were dislodged by trypsin treatment, re-suspended in a fresh 1mL growth media, and distributed equally (200μL each) among 5 wells of a 96-well plate (Catalog# 3912; Costar; Corning Inc.).

We confirmed the functionality of AMBER under physiological depolarization by co-expressing capsaicin activated rTRPV1 with FV-E-Y and luxCDE. We used $\approx$ 500ng of *pcDNA3.1-rTRAPV1* plasmid, $\approx$ 250ng of *FV-E-Y*, and $\approx$ 250ng of *luxCDE* for co-expressing rTRPV1 with the bright probe and its substrate producing proteins. The transfected cells were seeded onto a 12-well plate as before for bioluminescent imaging after capsaicin addition. For patch-clamp electrophysiology experiments, the transfected cells co-expressing the bright probe and its substrate were plated onto a PLL treated 13mm coverslip (Catalog# 63780-1; #1; 0.13-0.17mm; Electron Microscopy Sciences) placed inside each well of 12-well plate. We used a low seeding density ($\approx 10^4$cells) per well so that a sufficient single-cell population is available for electrical measurements.

1.4 Optical Imaging of HEK293 Cells Expressing Engineered Proteins

A custom imaging set up was built to record bioluminescent signals emitted by the engineered probes. We reduced the optical path between the sample and the detector by choosing a suitable inverted microscope (Tritech IX-512) that has a fewer number of components in the light path – an objective (Motic 10X 0.3 ¥/0.17) and a removable filter cube. A sensitive EMCCD (Electron Multiplied Charged Coupled Device) camera (back-illuminated Andor iXonEM+ 897, Mode# DU-897E-CSO-#BV) was directly mounted on the camera port fitted with a C-mount adapter. Acquired raw images were digitized with 512×512 pixels and transferred to a computer through a PCI controller card (CCI-23). The whole imaging setup was placed inside an Aluminum Faraday cage to minimize the influence of stray electromagnetic noise during recordings.

The EMCCD camera was operated using open-source Micromanager software v1.4 [11]. We cooled the CCD chip to -90^oC using an externally powered Peltier cooler to minimize the effect of thermal noise on the recordings. The camera has a high quantum efficiency over a wide spectral range (varies between 80-95% between 400-700 nm). A 12-well tissue culture plate containing attached transfected cells was fixed on a manual stage that allows precise in-plane positioning within a chosen field of view. We imaged cells in three different channels – bright field, fluorescence, and bioluminescence. All imaging experiments were performed at room temperature and stray ambient light was cut off using Blackout fabric (black Nylon, Polyurethane-coated; Thorlabs; Part# BK5) and Aluminum foils wherever necessary.

Bright-field images were recorded at very low illumination intensities. The pre-amplifier gain was set at 1× for a 10 MHz readout rate to eliminate the overflow of CCD registers. The exposure time was set at 5ms and the images were recorded at a small EM gain of 10. For fluorescent imaging, we used the same settings for pre-amplifier gain and the acquisition rate. However, the exposure time ($\approx$ 10-20 msec) and the EM gain (10-40) were varied between the samples depending on the expression level of the proteins.

Transient cellular expression of protein molecules was characterized using the YPet fluorescence (Tritech

Research; MINJ-F-FITC; Ex:480nm/Em:535nm). Endogenous NADH fluorescence was recorded in the DAPI channel (Tritech Research; MINJ-F-DAPI; Ex:350nm/Em:460nm) to characterize the O_2 concentration in cells before and after depolarization. NADH has a broad absorption peak ($\lambda_m$ax=350nm) and emission peaks [6]. The emission peak varies between ≈ 450-470 nm depending on whether NADH is in the free or bound state[6]. We did not discriminate the free/bound NADH signals in our experiments but rather report only the change in spectral mixing due to differential O_2 concentration.

We noticed cell-to-cell variability in protein expression besides the batch-to-batch variation. We observed the internalization of the probe molecules in less than 1% of the transfected cells that expressed proteins at high levels. More than 90% of the transfected cells in each batch expressed the probe proteins at moderate levels targeting the plasma membrane and are sensitized to bioluminescent emission under depolarization.

For bioluminescent imaging, the room was completely cut-off from the stray ambient light. We used a pre-amplifier gain of 5× and a readout rate of 3MHz. The exposure time was set at 10 sec for a maximum EM gain of 1000. Images were recorded before and after the addition of KCl (Sigma; Catalog# P9541-500G). Drops of KCl were added directly into the well without disturbing the field of view under focus. Bioluminescent images were recorded 10s immediately after the addition of KCl so that the cells imaged are not challenged for a longer duration. The DMEM media used contains 5mM of KCl. We, therefore, accounted for this amount in our estimates of the final concentration (≈ 50mM). The EMCCD camera is prone to show latency effect immediately after exposure to ambient light. We found a 10 sec delay allowed after KCl addition was sufficient to maintain a consistent basal noise floor without influencing the recordings with the latency effect. We also recorded the endogenous NADH fluorescence before and after the KCl addition.

For modeling physiological depolarization conditions, cells co-expressing rTRPV1, bright probe, and its substrate producing proteins were used for bioluminescent imaging. We activated rTRPV1 by adding Capsaicin (Sigma Aldrich; Catalog# M2028-250MG) at a final concentration of ≈ 100mM and allowed a 10s delay before recording the bioluminescent signals. The necessity to achieve a large depolarization within a short duration demanded a greater amount of Capsaicin in our assay (about 10× greater) than reported in the literature [4].

1.5 Bioluminescence Emission Spectra of AMBER and FV-E-Dark Mutant

Bioluminescence emission spectra of AMBER and FV-E-Dark constructs were obtained using plate reader equipment (Synergy H1, software version 3.00.19). All recordings were done at 37^oC with the recording probe positioned about 1mm from the top of the plate with a maximal gain value of 200. HEK293 cells co-expressing the AMER (or FV-E-Dark) and its substrate producing proteins (luxCDE) were used for the recordings after 48 hours post-transfection. Untransfected cells were used for negative control experiments. Firstly, we dark-adapted an opaque 96 well plate (Corning Inc; Costar; Catalog# 3912) by covering them with an Aluminum foil and stored them in a light cut-off dark ambiance for at least 12 hours. We found that the dark adaptation of the plate significantly improved the quality of the spectral traces by minimizing the stray emission during recordings. A dark-adapted plate containing cells suspended in growth media (200μL per well) was loaded on the instrument tray and thermally equilibrated for about 2 minutes at 37^oC. We recorded emission spectra between 400-600nm at a spectral resolution of 10nm allowing 10s integration time for each data point. Our experimental approach minimized the long-term effects of the KCl challenge on the bioluminescent signals by completion of the recordings within a short duration (≈ 3min). We obtained paired measurements by recording before and after KCl addition in each well. Median photons counts at each spectral wavelength were estimated from n= 8 samples within the chosen bandwidth. The raw data were then processed using curve-fitting models to tease out the bioluminescent signals of different constructs.

We used *a priori* knowledge of the background luminescence of HEK293 cells, luxAB emission and the YPet fluorescent emission spectra to curve fit a non-linear regression model that agrees closely with the median photon counts at each spectral wavelength obtained experimentally. Similar such approach was used earlier to quantify the scattering and fluorescent components of lipid-membrane complexes[39]. Figure S10 shows the recorded background luminescence of HEK293 cells suspended in the growth media, bioluminescent emission spectrum of iluxAB [16] and the fluorescent emission spectrum of YPet [23]. We digitized the iluxAB bioluminescent emission and the YPet fluorescent spectra using the open source WebplotDigitizer tool [31] to extract the relative coordinates of the spectra within a chosen bandwidth. Emission spectrum of *E. Coli* bacteria expressing iluxAB (derived from pl-luxAB) has a peak bioluminescent emission at $\lambda_{\max} \approx 490\mathrm{nm}$ [16] and is same as that of the eluxAB.

Curve fitting model for the emission spectrum of AMBER was represented as a linear weighted combination of three components - background luminescence, bacterial bioluminescence and YPet fluorescence. Weighted summation of these components account for the heterogeneous expression of AMBER proteins in HEK293 cells and non-radiative BRET emission from the eluxAB to the YPet.

$$\mathrm{I}(\lambda) = \mathrm{A.L}(\lambda) + \mathrm{B.Bk}(\lambda) + \mathrm{C.Yf}(\lambda) \tag{4.1}$$

where A, B and C are fitting constants that represent coefficients of eluxAB bioluminescence, background luminescence and YPet emission due to BRET coupling respectively. For FV-E-Dark mutant, the coefficient C=0, because the fluorescent property of the YPet is abrogated by mutational changes thereby preventing BRET component of the bioluminescent emission. Table S2 shows fitting constants of the spectral curve fits to the recordings of AMBER and FV-E-Dark mutant before and after KCl addition (See the SI Section 1.14). We improved the quality of the fits using the weighted-residual approach in which the computed weights are inversely proportional to the variance of the residues. This approach provides non-equal weights to each spectral data so that more importance is give to the data with least variability and vice versa. The coefficient of determination (R^2-adj > 0.99) was estimated to be close to the unity for both curve fits. We also evaluated 95% confidence interval of the emission for AMBER and FV-E-Dark mutant.

1.6 Characterizing AMBER Performance by Electrical Stimulation

We characterized the electro-optical performance of AMBER by determining the steady-state half-maximal voltage of the AMBER proteins using patch clamp experiments. Our experimental approach involves recording single cell bioluminescence of AMBER under a whole cell voltage clamp set up. HEK293 cells co-expressing AMBER were used for electrical stimulation after 48 hours post transfection.

Isolated single cells adhered onto a 13mm PLL treated coverslip (Catalog# 63780-1; #1; 0.13-0.17mm; Electron Microsccopy Sciences) were immersed into 150mL Ringers' bath solution added into an imaging chamber (Catalog# 64-1944; MODEL# QR-41LP; Quick release chamber for 18mm coverslips; Warner Instruments). The chemical composition of the bath solution (in mM): 140 NaCl, 5 KCl, 2 $\mathrm{CaCl_2}$, 1 $\mathrm{MgCl_2}$, 10 glucose, and 10 HEPES at pH 7.4 (adjusted with NaOH). Recording pipettes were pulled from a micropipette glass (Catalog# BF150-86-10; Borosilicate with filament OD 1.5 mm, ID 0.86 mm, 10cm length; Sutter Instruments) to 5 - 7 MΩ. Pipettes were filled with solution containing (in mM): 125 K-Gluconate, 8 NaCl, 0.6 $\mathrm{MgCl_2}$, 0.1 $\mathrm{CaCl_2}$, 1 EGTA, 10 HEPES, 4 Mg-ATP, 0.4 Na-GTP and pH 7.2 (adjusted with KOH). Cells showing sufficiently detectable YPet fluorescence were selected for patching in the whole-cell mode. A stable Giga Ohm seal was formed between a patch pipette and the cell membrane by spatially controlling the position of the patch pipette using micromanipulators (PCS-PS60, 5000 Series, Burleigh). Voltage clamping at different membrane potential was achieved using Axon 200B amplifier and 1440A Digitizer ($\mathrm{Axon_{TM}}$ Digidata 1550; Molecular Devices). The holding potential was stepped up from -60 mV to $+60$ mV in steps of $+20$ mV and then stepped back to -60 mV in steps of -20 mV. At each holding potential, bioluminescent intensity of the patched cell was recorded using an EMCCD camera (Andor iXonEM+ Ultra 897). We maintained the CCD chip at a sub-zero temperature ($\approx -90^o$C) using a Peltier cooler to minimize the thermal noise during the measurement. Single cell bioluminescent signals were recorded for 10sec at an acquisition rate of 1fps, readout rate of 3MHz and a maximum gain of 1000. We obtained paired measurements by recording the bioluminescent intensities of a patched cell for 6 independent repeats at various holding potentials within the chosen voltage range. We obtained the gating current transients by subtracting the resistive and capacitive leakage current transient from the total transient current obtained from the whole-cell electrical recordings (See Figure S11). First, we applied 20ms hyperpolarizing voltage steps from -70 mV to -90 mV at an incremental step of -10 mV from a holding potential of -60 mV. The correspondingly measured hyperpolarizing current traces consist of transient and steady-state components. As expected, the hyperpolarizing current transient agreed closely with a bi-exponential fitting model accounting for the pipette and membrane leakage currents. The resistance of the current path was determined applying Ohm's law to the steady-state current component. Membrane time constant was evaluated using the resistance and capacitance values obtained from the steady state and transient currents respectively. The on/off rates of the gating current transient were obtained by fitting a tri-exponential model to the total depolarizing transient current– pipette leakage component, membrane leakage component and a gating current component. We used previously determined membrane time constant values to obtain the fitting constants of all three components for depolarizing current transients. Depolarizing current transients were obtained by applying 20ms voltage steps from -60 mV to 60 mV at an incremental step of 20 mV from the holding potential of -60 mV. Gating current time constants were evaluated using the depolarizing current transients at the rising (falling) edge of the applied voltage steps.

Light kinetics recordings were obtained by conducting all-optical electrophysiology experiments. We sub-cloned a red light sensitive channel Rhodopsin variant (ReaCHR-Citrine) into a mammalian expression vector, pcDNA3.1 using standard molecular biology approaches. AAV-ReaCHR-Citrine was a gift from Roger Tsien laboratory (Addgene#50954; http://n2t.net/addgene:50954; RRID:Addgene_50954). HEK293 cells co-expressing AMBER and ReaCHR proteins were depolarized for 300ms by photoactivation of ReaCHR (λ= 630nm) and bioluminescent photons emitted by AMBER was recorded for the next 5s at a frame rate 20Hz.

1.7 Predictive Structural Modeling

Our cellular bioluminescent imaging experiments provide sufficient evidences to confirm the influence of BRET pair structure on the intensity of bioluminescence. We believe predicting the molecular structures of the BRET pairs - eluxAB-YPet and YPet-eluxAB will allow gaining structural insight into the AMBER function. Using I-TASSER computing tool [38], we identified the structural mechanisms underpinning the perturbation of the FMN pocket to predict the native folding of the BRET pairs. Structure of *V. harveyi* luxAB: FMN complex (PDB entry: 3FGC) was used as a basis [3] for comparison and screening of the candidates to identify the most likely predicted models with high confidence scores.

We quantified the hydrophobic properties of the previously identified FMN binding pocket defined by fourteen amino acids within the α subunit [25] - CYS106, ARG107, LEU109, TYR110, ARG125, VAL173, GLU175, SER176, THR179, ILE191, LEU192, SER193, TRP194 and SER227. These residues in vh-luxAB are conserved in the eluxAB sequence as well. Firstly, we quantified the solvent accessible surface area (SASA) [21] of the vh-luxAB FMN pocket in the bound state ($[\text{vh-luxAB}]^{\text{b}}_{\text{SA}}\approx 596.80\text{Å}^2$) to be slightly greater than that of the unbound state ($[\text{vh-luxAB}]^{\text{ub}}_{\text{SA}}\approx 558.45\text{Å}^2$) as reported previously [3]. In contrast, the FMN pocket size of the fused eluxAB (See Figure S9 for the fused eluxAB amino acid sequence) predicted by I-TASSER (Figure S14) is greatly reduced($[\text{eluxAB}]_{\text{SA}}\approx 345.14\text{Å}^2$). We attribute this contraction in the pocket size to the absence of association constraints between α and β subunits. Earlier work reported contact between the residues αPHE272 and βTYR151 is critical for the enzyme function. Disruption of this contact by substitution mutation almost abrogated the luxAB enzymatic activity. Most importantly, we found that the contact between αPHE272 and βTYR151 is achieved mainly due to the hydrophobic interaction at the interface of α and β subunits so that the residues can be shielded from the solvent environment. Detailed analysis of the measured inter-residue distances suggests the interaction at the interface of α and β subunits could be different under the FMN unbound and bound states (See Table S3). This finding supports our argument that interfacial constraints strongly influence the FMN pocket geometry of eluxAB and hence its enzymatic function.

We imposed the measured inter-residue distances as constraints of our predictive models solved using I-TASSER. Sequence alignment between vh-luxAB and eluxAB domains was also supplied as input because residues of eluxA domain and those located at the interfacial hydrophobic region were greatly conserved. Firstly, we predicted the fused eluxAB structure in the FMN unbound state by imposing the corresponding distance constraints shown in Table S3. Surprisingly, the FMN pocket of the predicted eluxAB opened up ($[\text{eluxAB}]^{\text{ub}}_{\text{SA}}\approx 618.75\text{Å}^2$) approximately close to that of the vh-luxAB structures. Furthermore, there was a negligible change (about 1%) in the FMN pocket size of the predicted eluxAB when bound state constraints were applied ($[\text{eluxAB}]^{\text{b}}_{\text{SA}}\approx 612.46\text{Å}^2$). For all practical reasons, this difference is negligible compared to the RMSD deviation between the predicted structures and their respective vh-luxAB counterparts. Our predicted model for the eluxAB provides a structural insight for the loss of the enzymatic activity if the association constraints are absent.

Our finding that FMN pocket geometry contracts in the absence of association constraints between the subunits is the key to the understanding of the structural basis of eluxAB (and its BRET pairs) function.

Next, we predicted the structures of the BRET pairs – eluxAB-YPet and YPet-eluxAB. Subunit interface distance constraints in the FMN unbound/bound states (listed under Table S3) were applied along with the sequence alignment information for computing the predicted models of the BRET pairs. Thermal mobility of FMN binding pocket residues was characterized using normalized B-factors obtained from the predicted I-TASSER models.

Mean free energy of solvation of the predicted molecules was computed using the approach described elsewhere [12]. The SASA values of the atomic species - N_1^+, C, N, O, O_1^- and S atoms were evaluated using the Visual Molecular Dynamics software plugin [21, 19]. Mean values of the atomic solvation parameters of the atomic species reported earlier [12] were used for estimating the free energies. Figure S16 shows the computed free energy barrier of the eluxAB, eluxAB-YPet and YPet-eluxAB molecules.

The FMN binding pocket of eLuxAB undergoes a profound change in its geometry depending on the relative position of YPet and eLuxAB (see Figure S15a). In particular, when YPet is placed at the N-terminus of eluxAB, the operating Förster distance was comparatively smaller ($\approx$43-45 Å) but at the expense of a major contraction of the FMN pocket in the unbound state (about $\approx 34.5\%$ lesser SASA than the bound state). This structural difference was correspondingly reflected in the high mean free energy difference of a thermodynamically unfavorable transition from the unbound to the bound state of YPet-eluxAB (estimated ($\Delta(\Delta G)$) ≈ 13.2 kcal/mol). In contrast, when YPet is placed at the C-terminus of eluxAB, its operating Förster distance becomes greater ($\approx$64-69 Å) but the FMN pocket geometry gets marginally affected in the unbound state (about $\approx 9.7\%$ lesser SASA than the bound state). This corresponds to a small free energy difference of a thermodynamically favorable transition ($\Delta(\Delta G)$)≈ -2.42 kcal/mol). We speculate the conformational change of VSD upon depolarization is sufficient to overcome the free energy barrier of eluxAB-YPet efficiently but not for the YPet-eluxAB. Albeit the transition is thermodynamically favorable, the free energy difference between the unbound and the bound state of eluxAB is sufficiently high (≈ -9.59 kcal/mol), which is why the fractional luminescence is negligible for V-E. Based on these analyses, we believe that modulating eluxAB activity by perturbing the FMN pocket geometry can be efficiently done when YPet movement is coordinated with eluxA through association constraints as opposed to direct interaction with the FMN pocket.

1.8 In vivo Expression of AMBER in *C. elegans*

We followed the protocols for *C. elegans* maintenance documented earlier [2]. Transgenic animals co-expressing the genetic elements of AMBER light machinery from high copy extra-chromosomal arrays were created using microinjection protocols described earlier [13, 27]. Briefly, plasmids encoding the bright probe and its substrate generating proteins at 50ng/µL each along with 100ng/µL pRF4 [rol-6(su104)] were injected into the distal gonads of well-fed day-1 or day-2 gravid adult hermaphrodites. We used *C. elegans* expression vectors with mec-7 and myo-2 promoters to drive the transgene expression in mechanosensory touch neurons and pharyngeal muscles respectively. We screened for Rol phenotype and YPet fluorescence in the transgenic F1 progeny and maintained those worms in separate plates. Transgenic animals from lines with high transmission of the extrachromosomal arrays were subsequently analyzed for expression of the bioluminescent reporters.

We selected lines exhibiting Rol phenotype that show YPet fluorescent signal for in vivo bioluminescent imaging. Surprisingly, myo-2 driven expression in the Rol phenotype animals showed stronger YPet fluorescence targeting pharyngeal muscles compared to the mec-7 driven expression in touch neurons.

1.9 Approach For Tracking *C. elegans* During Voltage Imaging

Limited photon budget of bioluminescent reaction demands long camera exposure times at high gain to detect the signal. Live tracking of the position and shape changes of an animal is required for spatially mapping the activity in real-time. We developed an imaging approach to track the spatial information of a freely moving animal by time-gating the bioluminescent recordings in each exposure cycle. Sacrificing bioluminescent photons temporally at this gated interval (< 10ms) in each exposure cycle practically will not affect the time-integrated bioluminescent intensities.

We performed live functional imaging of *C. elegans* using an inverted microscope (TRITECH IX-512) mounted with an EMCCD camera (Andor iXonEM+ 897). The image sensor of the camera was thermoelectrically cooled to -90°C. Our in vivo imaging assay requires alternating between the bright field (low gain and small exposure time) and the bioluminescent (high gain and long exposure time) recording modes so that the shape changes and the position of the animal can be tracked simultaneously while detecting bioluminescent signal. A similar approach was used for simultaneous tracking of the neural gene expression and behavior of marmosets at a higher frame rate[20]. We accomplished this using a custom-made set up that allows our camera exposure to be synchronized with a light emitting diode (LED) illumination during the bright field exposure. A micromanager script that instructs the camera to perform a particular exposure sequence alternating between bioluminescent and brightfield modes was developed. Execution of that script delivers a trigger voltage to a microcontroller (Arduino Uno Rev.3) that drives a flash circuit (a 2N7000 transistor and a 330 Ohm resistor) to illuminate an LED (Adafruit Super bright white 5mm; Product ID#754) selectively during brightfield image acquisition. The LED is positioned relative to the sample at a distance so there is no latency while recording the bioluminescent signals.

We exploited orders of difference in the exposure times and gains between the bright field and bioluminescent imaging modes to develop an algorithm for live tracking. Figure S17a shows the connectivity and circuit diagram between different components of the imaging hardware. The flow chart (Figure S17b) explains an algorithm applied for programming the microcontroller hardware. We start the image acquisition by running a micromanager script (see *imcapture.bsh* in the SI Section 1.14) that instructs the camera to follow a programmed exposure pattern (blue for the luminescence and black for the bright field) as shown in Figure S17c. The camera exposure pattern alternates between bioluminescence and bright field modes generating trigger voltage consistent with the exposure times. We programmed the microcontroller using the *a priori* knowledge that a short pulse always follows a long pulse (See *MicroscopeLight.ino* in the SI Section 1.14). This ensures that the lighting patterns driven by the microcontroller follows synchronously with the camera trigger output (set in the 'imcapture.bsh'). Initially, the microcontroller was set in the 'idle state' waiting for a rising edge of a pulse. After encountering the rising edge of a pulse, it evaluates if the pulse width (grey color) was greater than $\mathrm{t_L}/2$ ($\approx$ 0.25-0.5 sec). If so, the microcontroller will switch to 'arm state' waiting for the next rising edge to drive the flash circuit. Once the rising edge of the bright field trace is detected, the LED is turned on instantaneously during the period of bright field exposure ($\mathrm{t_S} < 10$msec). The LED turns off once the falling edge is approached resetting the microcontroller to the 'idle-state' again to encounter the next pulse. We ignored the time for communicating between different hardware during the image acquisition because the bioluminescent photons if any, lost during this time are negligible.

1.10 Recording *C. elegans* Pharyngeal Muscle Activity using AMBER

We demonstrated the in vivo use of AMBER using *C. elegans* animal model. We imaged the voltage activities of the pharyngeal muscles - electropharyngeogram (EPG) and the terminal bulb action potential (AP) using our custom-built imaging set up. Transgenic animals (1-3 days old) constitutively co-expressing the bright probe and its substrate in the pharyngeal muscles were used for these experiments. We transferred the animals on to a thin LB agar bed created on a glass coverslip (Catalog# 72210-21; Electron Microscopy Sciences) using a flame sterilized platinum wire. Bioluminescent voltage signals of *C. elegans* pharynx were recorded under two different conditions – bacterial feeding and stimulated starvation. For bacterial feeding, the agar bed was sufficiently loaded with $\mathrm{OP_{50}}$ bacteria locally for the worms to feed so that their movements are restricted within the chosen field of view. For recording under stimulated starvation, transgenic animals were transferred onto an agar bed after treatment with $\approx$ 50mM serotonin for 20 minutes. The animals were allowed to acclimatize in the new environment for about 15 minutes before starting the imaging protocol. Under both these experimental conditions, we did not observe any gross physical movements (limited to a spatial resolution of about $\approx 8\mu$m/pixel) of the body of the imaged animals except for their small head movements restricted to a radius of 2 to 3 pixels.

Live bioluminescent imaging of animals was performed using our custom-built imaging set up described in the earlier section. We used two different objectives (Plan 4X $0.1\infty/-$ and Motic 10X $0.3\infty/0.17$) in our imaging experiments. High expression of probe molecules enabled to use 10X objective for imaging a few animals. Transgenic animals loaded on the agar bed created on a coverslip were positioned over the objective using a mechanical stage. The imaging room was completely light cut-off using aluminum foil sheets and black fabric. We captured 200 frames each in bioluminescent and bright field modes alternatively. The programmed exposure trace consists of two alternating exposure times at a 3MHz readout rate - 1sec at a maximum gain of 1000 and 5 msec at a lower gain of 20. A total of 400 frames (200 frames each containing bioluminescent and bright field images) were recorded using different magnifications. Figure S17c shows the exposure pattern used for one such experiment with $\mathrm{t_L}$ = 0.5-1 sec and $\mathrm{t_S}$= 6 msec. The raw intensity data obtained were processed further to obtain the optical characterization of the pharyngeal pumping events of animals.

Bioluminescent readout is generally weak and requires integration of the signal over a finite time interval to detect with high confidence. We, therefore, developed a technique to extract the fast kinetics from the time-integrated response obtained at a slow frame rate. Put simply, this approach enables reconstructing an *a priori* fast kinetic signature using random uncorrelated slow kinetic data sets obtained from asynchronous measurements of repetitively conducted experiments. Consider a trajectory of a projectile described mathematically in the form of a parabolic path. Assume, we record the trajectory of the projectile using a slow speed camera that then we end up capturing a very few instantaneous locations along the parabolic path. Joining these locations with lines gives a reduced representation of the path that is far simpler than the actual ground truth parabolic path. In other words, the signal to noise ratio is so high because lesser number of samples were used to describe the representative path. What if the experiment is repeated multiple times and each time if the instantaneous location of the projectile along the parabolic path was randomly captured? Then for a certain large number of samples, one would be able to reconstruct a representative trace that is very close to the ground truth parabolic path.

Our technique relies on sparse sampling approach that is used in the field of signal processing. Several variants of sparse sampling approach are now being applied for image processing [22, 26] as well. We modified a recently published technique [26] that used slow frame rate imaging to capture the fast neuronal kinetics. Unlike, the instantaneously recorded signals used in the earlier work [26], our approach use multiple temporally integrated bioluminescent voltage signals recorded at regular intervals for reconstructing the representation of the ground truth signals. Using this technique, we teased out the EPG and AP traces of the animals using hundreds of time integrated samples of data recorded under bacterial feeding and stimulated starvation conditions.

We developed a MATLAB (R2020b) program (See *stcfiltfun.m* in the SI Section 1.14) for reconstructing the EPG traces of animals under different conditions using our modified sparse sampling approach. Figure S18 shows a flow chart that explains the key steps of our approach. Firstly, we digitized the coordinates of an EPG trace reported previously in [9] to generate a 500 msec trace using WebplotDigitizer tool [31]. The duration of an EPG trace within the 500 msec window is ≈ 250msec and no two EPG signatures occurs within a 500 msec time window. Next, we convolved the digitized EPG trace with a 500 msec random noisy signal. The total duration of the resultant noise-convolved data (≈ 1sec) is approximately four times the duration of the fast kinetics of the pharynx. EPG convolution with random noise is an irreversible operation and the original trace cannot be retrieved by differentiation (See Figure S19). We then generated n stimulation traces by randomly selecting a 500 msec window from the noise-convolved signal generated for ≈ 1 sec. We assigned these n stimulation traces to the n time-integrated bioluminescent signals recorded from the animals under different conditions. Generation of this stimulation data set is based on random selection of the central location of the window. Random selection made at the extremities of noise-convolved window (< 250 msec on either sides) was replaced by 500 msec trace located at the corresponding extreme location. We evaluated response-weighted covariance matrix, [C] (similar to the spike-triggered covariance [35]) using area normalization of individual stimulant profile. This step ensures unbiased assignment of equal stimulation strength to each of the recorded voltage response.

$$[C] = \frac{1}{n-1}\sum_{i=0}^{n} R_i.(S_i - \bar{S}).(S_i - \bar{S})^T - S_i.S_i^T \tag{9.1}$$

where R_i , S_i , $\bar{S}$, and, n are experimentally recorded individual bioluminescent response, unbiased stimulation vector assigned, the mean stimulation vector and the total number of responses respectively. The superscript T denotes transpose of the vector. Finally, we computed Eigen solutions of [C] to determine the vector component associated with the maximal covariance in a reduced dimension. Eigen vector components corresponding to the maximum Eigen value represents the time-integrated EPG trace of the animal within the chosen time window. Derivative of this trace gives a representation of the ground truth signal.

Fidelity of the reconstruction is not arbitrary and depends on the quality of the time-integrated bioluminescent voltage signals recorded. This was confirmed by supplying random input to our MATLAB code, which generated a random and uncorrelated output (See Figure S19). In contrast, when temporally integrated voltage signals were supplied, the program precisely predicted a representative trace approximately close to the ground truth signal. However, the SNR of the representative trace depends on the number of sampling points supplied to reconstruct the trace. SNR improves significantly when the sample size is increased after bootstrap with replacement.

We also reconstructed the terminal bulb AP using the bioluminescent voltage signals obtained from the terminal bulb of the animals (See Figure S20). We digitized [31] electrically recorded terminal bulb AP reported previously [8] to generate the input for the MATLAB program.

1.11 Voltage Imaging of *C. elegans* Touch Neurons Activities Using AMBER

We used AMBER to visualize the activities of mechanosensory touch neurons in freely moving *C. elegans*. Firstly, we assessed the efficacy of targeting mechanosensory touch neurons by fluorescent imaging of transgenic worms expressing the eGFP protein driven by the mec-7 promoter (Figure S21). Epifluorescent images of the animals expressing eGFP gene driven by mec-7 promoter were acquired using a Nikon Eclipse Ti microscope controlled by NIS Elements AR software. Specimens were illuminated with an X-cite light source using a GFP filter (480/40 bandpass excitation filter). Images were recorded using a Hamamatsu CMOS sensor through a 20X objective. The mec-7 promoter targets the touch neurons identified earlier [32] – PLM (L/R), PVM, ALM (L/R), AVM and anterior nerve ring (NR). eGFP was expressed at high levels in most of the touch neurons (PLM, PVM, ALM, AVM and NR). Expression in PVD was relatively lower compared to other touch neurons. Transgenic animals (1-3 days old) constitutively expressing the bright probe and its substrate genes driven by mec-7 promoter were used for the bioluminescent imaging experiments.

Our functional bioluminescent imaging approach involves tracking the spatial locations of the moving animals simultaneously while recording bioluminescent signals using a custom-built imaging set up described in the earlier section. We used a 4X objective (Plan 4X $0.1\infty/-$) to achieve a greater field of view so that the movements of the worms can be tracked over a large distance. Animals moving randomly over a bacterial lawn created on an agar bed inside a 10cm dish were positioned over the objective of the inverted microscope using a mechanical stage. The imaging room was completely light cut-off and all recordings were taken at room temperature. We captured 200 frames each in bioluminescent and bright field imaging modes alternatively. Bioluminescent images were recorded exposing the image sensor for 1s at a maximum gain (1000) and a minimum readout speed (3 MHz). The intervening bright field images were captured exposing the image sensor for 6msec at a very low gain (20) immediately after each bioluminescent frame. Several image stacks containing 400 frames (200 frames each with bioluminescent and bright field images) were captured to detect the activity of the touch neurons as reported under different conditions. Figure S17c shows the exposure pattern used for one such experiment with $\mathrm{t_L} = 1$ sec and $\mathrm{t_S} = 6$ msec. The raw intensity data obtained from the image stacks using this approach were processed to map different touch neurons of freely moving multiple animals.

1.12 Image and Data Processing Methods

We post-processed raw bioluminescent micrographs to determine the true signal intensities. We used the open-source ImageJ software (ImageJ 1.52p) to post-process all the recorded images [33]. Raw bioluminescent micrographs (512×512 pixels) from the cell culture experiments were binned spatially (4×4) to increase the signal-to-noise ratio of bioluminescent intensity. We found a 4×4 spatial binning was sufficient to achieve the discern able signal output without substantially compromising the resolution of the morphological features spatially. The resulting 128×128 pixel images were background subtracted (Process → Subtract Background) applying a rolling ball radius of 50 pixels. This was followed by the removal of bright signal outliers (Process → Noise → Remove Outliers) at a radius of 2 pixels and a threshold intensity of 50 a.u. The resulting images were then despeckled (Process → Noise → Despeckle) to remove speckle patterns if any in the field of view. The images were finally digitized for 16-bit color code to compute the differential change in the bioluminescent signal intensity, $\Delta\mathrm{L/L}$ for each pixel. We noticed that the maximum bioluminescent intensity of cells expressing different engineered proteins vary over a wide range after depolarization. We therefore formulated a new metric termed normalized differential luminescence, $(\Delta\mathrm{L/L})^{\mathrm{n}}$ to compare the bioluminescent performance of different engineered AMBER protein constructs.

$$(\Delta \mathrm{L/L})^{\mathrm{n}} = (\Delta \mathrm{L/L}) \times \frac{\mathrm{I^d} \times \mathrm{t_b^d}}{\mathrm{I_b^d} \times \mathrm{t^d}} \tag{11.1}$$

where $\mathrm{I_d}$ and $\mathrm{t_d}$ are the mean differential bioluminescent intensity and integration time of the samples expressing different engineered protein constructs and $\mathrm{I_b^d}$ and $\mathrm{t_b^d}$ are the mean differential bioluminescent intensity and the integration time (10 sec) of the AMBER construct.

We developed an image processing protocol to generate movies that show live spatial tracking of bioluminescent intensities in a freely moving animal. Image stacks containing bioluminescence and brightfield frames alternatively were post-processed to create animated movies. Image stacks were segregated into brightfield and luminescent substacks using ImageJ built-in function (Image → Stacks → Tools → Make Substack). We used different ranges in the substack maker to create these two different substacks 200 frames each – (1-399-2) for bioluminescence and (2-400-2) for brightfield. A moving window with time-integrated pixel intensities for 10sec stepping up at 1sec increment along the time axis was applied to process the individual frames of the bioluminescent stack. This was done using an AWK programming script (See *slicegen.awk* in the SI Section 13), whose output generates an ImageJ macro that performs the time integration of pixel intensities. Execution of this ImageJ script generated a modified substack with 189 frames of temporally integrated bioluminescent intensities (10 sec integration time) at 1s increment. The modified substack was background subtracted followed by thresholding the intensity contours at the maximum background intensity to obtain the spatially graded bioluminescent signals at different time points. We then mapped the bioluminescent signals to the spatially binned (4×4) brightfield stack using an ImageJ plugin (Stack Interleaver) developed earlier [5]. This method was applied to spatially map the bioluminescent intensities of freely moving transgenic animals to the corresponding brightfield image recorded at that instant.

We characterized the voltage activity of the pharyngeal muscles of free unrestrained individual animals. Weak background signal from the embryos inside young hermaphrodite adults was confirmed both from the fluorescent and bioluminescent recordings. Live animal tracking protocol discussed before was used to create movies showing pharyngeal muscle activities of young adults for a few minutes. Movies depicting the temporally integrated electrical activity of the pharyngeal muscles agreed with the dynamical trend reported earlier [18]. No gross physical movements of the animals were observed while recording the pharyngeal muscle activities of the animals. Using MATLAB programming (See *sctfiltfun.m* in the SI Section 1.14), we processed the raw bioluminescent voltage signals recorded for 100 sec from several animals (and under different conditions) to reconstruct the representation of the ground truth electropharyngeogram (EPG) and the Terminal Bulb Action Potential (AP).

Movies showing mechanosensory touch neurons activities of animals were created cropping a window that includes a complete field of view of the motion trajectories. We observed spatial distribution of the bioluminescent intensities representing different levels of activity in the moving animals. However, the number of pixels coding the fractional intensity varied spatiotemporally at the predetermined locations. These locations presumably agreed with soma of the mechanosensory touch neurons mapped by fluorescent imaging (Figure S21). Similar recordings from untransfected control animals did not give any detectable voltage signals for the chosen threshold intensity values thereby confirming the recorded intensities correspond to the mechanosensory behavioural cues. We observed varying levels activity of the touch neuronal circuit temporally during burst reversal. We do not know if the signal retention due to time integration or the effect of animal body contraction influence the observed voltage activity.

1.13 Cell Viability Assay

We characterized the effect of transgene expression if any, on the viability of HEK293 cells using Thiazolyl Blue Tetrazolium Bromide (MTT, Sigma Aldrich, Catalog# 5655-100MG) assay [28]. Briefly, the experiment involves transfecting $\approx 10^6$ HEK293 cells with 1μg of plasmid DNA using Lipofectamine transfection reagent as described under Section 2. After 48 hours post-transfection, adherent transfected cells from a 60mm dish were dislodged by trypsin treatment ($\approx 500\mu$L) followed by two successive wash steps with freshly prepared growth media. We then suspended the cells in 1mL of Ringers' solution because DMEM interferes with the absorbance measurements in the optical wavelength regime of MTT assay. Cells suspended in Ringers' solution were mixed with MTT to a final concentration of 0.5% and 180μL of the mixture was loaded into

5 wells of a 96-well tissue culture plate (Falcon 96 flat bottom clear). The plate was left inside the tissue culture incubator maintained at 37^{o}C and 87%RH for 4 hours. MTT is a metabolic activity indicator because mitochondrial dehydrogenases of living cell coverts MTT (yellow colored water-soluble substance with low optical absorbance at 570nm) into Formazan (blue water-insoluble precipitate with high optical absorbance at 570nm). After 4 hours, we added 20μL of solvent (10% of Triton X-100 in acidified isopropanol containing 0.1N HCl) to dissolve the insoluble Formazan settled at the bottom of the reaction wells. The plate was again placed inside the tissue culture incubator maintained at 37^{o}C and 87%RH overnight to completely solubilize the product of the reaction. We used untransfected HEK293 cells and MTT dissolved in Ringers' solution without cells as positive and negative controls of the experiment.

Optical measurements were taken using a plate reader (Synergy H1, software version 3.00.19) and all recordings were done at 37^{o}C after a brief linear shaking for 3sec. We measured the endpoint absorbance values of the samples in each well at the assay wavelength (570 nm) and the reference wavelength (670 nm). Figure S22 shows a plot comparing the absorbance values of the experimental and control samples. We observed a very small change in the absorbance of the samples expressing the AMBER genes and those treated with the Lipofectamine reagent only- a maximum drop of 9.2% for cells expressing the substrate genes alone when transfected with 1μg of DNA. We noticed this effect proportionately drops to 4.5% in co-transfected samples perhaps due to reduction in the amount of substrate plasmid DNA to 500ng. The expression of probe genes does not seem to have any major influence on the cell viability ($\approx$ 4% drop with respect to Lipfectamine treated cells). Our estimates of the viability characterization correspond to the upper bound because empty vector alone was reported to have some marginal effect. Given these considerations, we believe that the influence of transgene expression on the cell viability is very negligible. As expected, both positive and negative control samples reported the highest and the lowest absorbance values respectively.

1.14 Scripts and Macros

1.14.1 MATLAB program for evaluating curve fitting constants of the AMBER and FV-E-Dark Mutant

```
% MATLAB Code for Computing Coeffcients of AMBER Spectra
 clear;
 close all;
% Reference iluxAB spectrum (Stefan Hell PNAS 2018)
lux_ref = readtable(’luxAB_Spectrum.txt’);
lambda_ref = lux_ref.Wavelength;
BioL_ref=normalize(lux_ref.Bioluminesence,’range’);
% Background Media Luminesence
bkgnd = readtable(’background_spectra.txt’);
lambda_Bk = bkgnd.Wavelength;
Bk_BioL = [bkgnd.T1,bkgnd.T2,bkgnd.T3,bkgnd.T4];
%Bootstrap Sample
Boot_Bk=bootstrp(1000,@median,Bk_BioL’);
mean_Bk_T= normalize(median(Boot_Bk,1),’range’);
mean_Bk=mean_Bk_T’;
Prcnt_Bk=prctile(Bk_BioL,[5,95],2);
%YPet Data from FPbase.org
YPET=readtable(’YPET_data.txt’);
YPET_lambda = YPET.Wavelength;
YPET_Fl = YPET.Intensity;
%Amber Data
Amb_No_KCl = readtable(’AMBER_no_KCl.txt’);
Amb_KCl = readtable(’AMBER_KCl.txt’);
lambda_Amb_no_KCl = Amb_No_KCl.Wavelength;
lambda_Amb_KCl = Amb_KCl.Wavelength;
BioL_Amb_no_KCl=[Amb_No_KCl.T1,Amb_No_KCl.T2,Amb_No_KCl.T3,Amb_No_KCl.T4,Amb_No_KCl.T5,
Amb_No_KCl.T6,Amb_No_KCl.T7,Amb_No_KCl.T8,Amb_No_KCl.T9,Amb_No_KCl.T10,Amb_No_KCl.T11,
Amb_No_KCl.T12,Amb_No_KCl.T13,Amb_No_KCl.T14];
Boot_Biol_Amb_no_KCl=bootstrp(5000,@median,BioL_Amb_no_KCl’);
Mean_Biol_Amb_no_KCl_T=normalize(median(Boot_Biol_Amb_no_KCl,1),’range’);
Mean_Biol_Amb_no_KCl= filloutliers(Mean_Biol_Amb_no_KCl_T’,’clip’,’movmedian’,50,
’SamplePoints’,lambda_Amb_no_KCl);
```

```
BioL_Amb_KCl=[Amb_KCl.T1,Amb_KCl.T2,Amb_KCl.T3,Amb_KCl.T4,Amb_KCl.T5,Amb_KCl.T6,
Amb_KCl.T7,Amb_KCl.T8,Amb_KCl.T9,Amb_KCl.T10,Amb_KCl.T11,Amb_KCl.T12,Amb_KCl.T13,
Amb_KCl.T14];
Boot_Biol_Amb_KCl=bootstrp(5000,@median,BioL_Amb_KCl');
Mean_Biol_Amb_KCl_T=normalize(median(Boot_Biol_Amb_KCl,1),'range');
Mean_Biol_Amb_KCl= Mean_Biol_Amb_KCl_T';
%Calculate 95% confidence intervals
Prcnt_BioL_Amb_KCl=prctile(Boot_Biol_Amb_KCl',[5,95],2);
%Interpolte data for a better fit
resmp_ratio = 2;
resmp_mean_Bk = smooth(interp(mean_Bk,resmp_ratio),3,'sgolay',1);
resmp_lambda_Bk=interp(lambda_Bk,resmp_ratio);
resmp_YPET_lambda = interp(YPET_lambda,resmp_ratio);
resmp_YPET_FL = interp(YPET_Fl,resmp_ratio);
resmp_Mean_Biol_Amb_KCl = smooth(interp(Mean_Biol_Amb_KCl,resmp_ratio),5,'sgolay',1);
resmp_lambda_Amb_KCl = interp(lambda_Amb_KCl,resmp_ratio);
resmp_lambda_Amb_no_KCl = interp(lambda_Amb_no_KCl,resmp_ratio);
resmp_Mean_Biol_Amb_no_KCl = smooth(interp(Mean_Biol_Amb_no_KCl,resmp_ratio),5,'sgolay',1);
resmp_lambda_ref = interp(lambda_ref,resmp_ratio);
resmp_BioL_ref = interp(BioL_ref,resmp_ratio);
%Background Fit Function
[Bkgnd, goodness, output] = fit(resmp_lambda_Bk,resmp_mean_Bk,'smoothingspline');
%Bioluminesence Reference Fit Function
[biolum_ref,goodness2,output2] = fit(resmp_lambda_ref,resmp_BioL_ref,'smoothingspline');
%YPet Fit Function
[ypet_fl, goodness4, output4] = fit(resmp_YPET_lambda,resmp_YPET_FL,'smoothingspline');
% Predicted Fit Function
myfit_fn = fittype(@(A,B,C,x) A.*biolum_ref(x)+B.*Bkgnd(x)+C.*ypet_fl(x),'independent','x',
'coefficients', {'A','B','C'});
% Initial Fit
[fitBioAKINI,RAKINI,op3]=fit(resmp_lambda_Amb_KCl,resmp_Mean_Biol_Amb_KCl,myfit_fn,
'Lower',[0,0,0]);
[fitBioAnKINI,RAnKINI,op4]=fit(resmp_lambda_Amb_no_KCl,
resmp_Mean_Biol_Amb_no_KCl,myfit_fn,'Lower',[0,0,0]);
%Compute Weights
w2=(op3.residuals-mean(op3.residuals)).^-2;
w3=(op4.residuals-mean(op4.residuals)).^-2;
%refit with Weighting
[fitBioAK,RAK,op6]=fit(resmp_lambda_Amb_KCl,resmp_Mean_Biol_Amb_KCl,myfit_fn,
'Weight',w2,'Lower',[0,0,0]);
[fitBioANK,RAnK,op7]=fit(resmp_lambda_Amb_no_KCl,resmp_Mean_Biol_Amb_no_KCl,myfit_fn,
'Weight',w3,'Lower',[0,0,0]);
%Find Fit Coefficients for Amber with KCl
coeff_res = coeffvalues(fitBioAK);
A1=coeff_res(1);
B1=coeff_res(2);
C1=coeff_res(3);
%Compute Confidence Interval
Conf_IntAK=confint(fitBioAK);
%Compute Predicted Function
Pred_Amb_K = A1.*biolum_ref(resmp_lambda_Amb_KCl)+B1.*Bkgnd(resmp_lambda_Amb_KCl)
+C1.*ypet_fl(resmp_lambda_Amb_KCl);
Pred_Amb_K_low=Conf_IntAK(1,1).*biolum_ref(resmp_lambda_Amb_KCl)+
Conf_IntAK(1,2).*Bkgnd(resmp_lambda_Amb_KCl)+
Conf_IntAK(1,3).*ypet_fl(resmp_lambda_Amb_KCl);
Pred_Amb_K_high=Conf_IntAK(2,1).*biolum_ref(resmp_lambda_Amb_KCl)+
Conf_IntAK(2,2).*Bkgnd(resmp_lambda_Amb_KCl)+
Conf_IntAK(2,3).*ypet_fl(resmp_lambda_Amb_KCl);
%Plot Amber KCl Prediction
figure(1)
plot(lambda_Amb_KCl,Mean_Biol_Amb_KCl,'*',resmp_lambda_Amb_KCl,
resmp_Mean_Biol_Amb_KCl,'o',
resmp_lambda_Amb_KCl,Pred_Amb_K,resmp_lambda_Amb_KCl,Pred_Amb_K_high,'--',
resmp_lambda_Amb_KCl,Pred_Amb_K_low,'--');
%Find Fit Coefficients for Amber without KCl
```

```
coeff_res = coeffvalues(fitBioANK);
AN1=coeff_res(1);
BN1=coeff_res(2);
CN1=coeff_res(3);
Conf_IntAnK=confint(fitBioANK);
%Compute Predicted Function
Pred_Amb_no_K = AN1.*biolum_ref(resmp_lambda_Amb_KCl)+BN1.*Bkgnd(resmp_lambda_Amb_KCl)+
CN1.*ypet_fl(resmp_lambda_Amb_KCl);
Pred_Amb_no_K_low=Conf_IntAnK(1,1).*biolum_ref(resmp_lambda_Amb_KCl)+
Conf_IntAnK(1,2).*Bkgnd(resmp_lambda_Amb_KCl)+
Conf_IntAnK(1,3).*ypet_fl(resmp_lambda_Amb_KCl);
Pred_Amb_no_K_high=Conf_IntAnK(2,1).*biolum_ref(resmp_lambda_Amb_KCl)+
Conf_IntAnK(2,2).*Bkgnd(resmp_lambda_Amb_KCl)+
Conf_IntAnK(2,3).*ypet_fl(resmp_lambda_Amb_KCl);
%Plot Amber without KCl Prediction
figure(2)
plot(resmp_lambda_Amb_no_KCl,resmp_Mean_Biol_Amb_no_KCl,’o’,
resmp_lambda_Amb_KCl,Pred_Amb_no_K,
resmp_lambda_Amb_KCl,Pred_Amb_no_K_high,’--’,
resmp_lambda_Amb_KCl,Pred_Amb_no_K_low,’--’);
%Plot only Biolum & Ypet for both KCl and No KCl
figure(3)
resmp_lambda_Amb_KCl = interp(lambda_Amb_KCl,3);
Mean_Amb_K=(A1).*biolum_ref(resmp_lambda_Amb_KCl)+(C1).*ypet_fl(resmp_lambda_Amb_KCl);
Mean_Amb_K_Hi=Conf_IntAK(2,1).*biolum_ref(resmp_lambda_Amb_KCl)+
Conf_IntAK(2,3).*ypet_fl(resmp_lambda_Amb_KCl);
Mean_Amb_K_Lo=Conf_IntAK(1,1).*biolum_ref(resmp_lambda_Amb_KCl)+
Conf_IntAK(1,3).*ypet_fl(resmp_lambda_Amb_KCl);
Err_K=[Mean_Amb_K_Hi-Mean_Amb_K,Mean_Amb_K-Mean_Amb_K_Lo];
Mean_Amb_no_K=(AN1).*biolum_ref(resmp_lambda_Amb_KCl)+
(CN1).*ypet_fl(resmp_lambda_Amb_KCl);
Mean_Amb_no_K_Hi=Conf_IntAnK(2,1).*biolum_ref(resmp_lambda_Amb_KCl)+
Conf_IntAnK(2,3).*ypet_fl(resmp_lambda_Amb_KCl);
Mean_Amb_no_K_Lo=Conf_IntAnK(1,1).*biolum_ref(resmp_lambda_Amb_KCl)+
Conf_IntAnK(1,3).*ypet_fl(resmp_lambda_Amb_KCl);
Err_no_K=[Mean_Amb_no_K_Hi-Mean_Amb_no_K,Mean_Amb_no_K-Mean_Amb_no_K_Lo];
bounds =[Mean_Amb_K_Lo’;Mean_Amb_K_Hi’];
boundedline(resmp_lambda_Amb_KCl,Mean_Amb_K,Err_K,’alpha’)
hold on;
boundedline(resmp_lambda_Amb_KCl,Mean_Amb_no_K,Err_no_K,’r’,’alpha’)
hold off;
%%%%%%%%%%%%%%%%%%%%%%%%%%%%%%%%%%%%%%%%%%%%%%%%%%%%%%%%%%%%%%%%%%%%%%%%%%%
clear;
close all;
% Read data
bkgnd = readtable(’background_spectra.txt’);%Background Spectrum
luxop=readtable(’lux_oper_spectra.txt’);%soluble eluxAB Data
lux_ref = readtable(’luxAB_Spectrum.txt’);%Reference luxAB spectrum
(from ilux Stefan Hell PNAS 2018)
lux_dark_No_KCl = readtable(’Dark_no_KCl.txt’);% Dark Mutant Data before KCl depolarization
lux_dark_KCl = readtable(’Dark_Kcl_spectra.txt’);% Dark Mutant After KCl depolarization
resmp_ratio = 5;
%Create Data Matrices
lambda_ref = lux_ref.Wavelength;
BioL_ref=normalize(lux_ref.Bioluminesence,’range’);
lambda_lux = luxop.Wavelength;
Lux_BioL = [luxop.T1,luxop.T2,luxop.T3,luxop.T4] ;
data_lux = normalize(median(Lux_BioL,2),’range’);
lambda_Bk = bkgnd.Wavelength;
Bk_BioL = [bkgnd.T1,bkgnd.T2,bkgnd.T3,bkgnd.T4];
resmp_lambda_Bk=interp(lambda_Bk,resmp_ratio);
resmp_lambda_lux = interp(lambda_lux,resmp_ratio);
lambda_dark_No_KCl = lux_dark_No_KCl.Wavelength;
lambda_dark_KCl = lux_dark_KCl.Wavelength;
BioL_dark_no_KCl=[lux_dark_No_KCl.T1,lux_dark_No_KCl.T2,lux_dark_No_KCl.T3,
```

```
lux_dark_No_KCl.T4,lux_dark_No_KCl.T5,lux_dark_No_KCl.T6,lux_dark_No_KCl.T7,
lux_dark_No_KCl.T8,lux_dark_No_KCl.T9];
BioL_dark_KCl=[lux_dark_KCl.T1,lux_dark_KCl.T2,lux_dark_KCl.T3,lux_dark_KCl.T4,
lux_dark_KCl.T5,lux_dark_KCl.T6,lux_dark_KCl.T7,lux_dark_KCl.T8,lux_dark_KCl.T9,
lux_dark_KCl.T10,lux_dark_KCl.T11,lux_dark_KCl.T12,lux_dark_KCl.T13,lux_dark_KCl.T14];
%Bootstrap Resample Data
%Background
Boot_Bk=bootstrp(5000,@median,Bk_BioL');
mean_Bk_T= normalize(median(Boot_Bk,1),'range');
mean_Bk=smooth(interp(mean_Bk_T',resmp_ratio),25,'sgolay',5);
%Cytosolic fused eluxAB
Boot_lux=bootstrp(5000,@median,Lux_BioL');
mean_lux_T=normalize(median(Boot_lux,1),'range');
mean_lux=smooth(interp(mean_lux_T',resmp_ratio),25,'sgolay',2);
%Create Background Fit function
[Bkgnd, goodness, output] = fit(resmp_lambda_Bk,mean_Bk,'smoothingspline');
[biolum_ref,goodness2,output2] = fit(lambda_ref,BioL_ref,'smoothingspline');
myfit_fn = fittype(@(A,B,x) (A.*biolum_ref(x))+(B.*Bkgnd(x)),'independent','x',
'coefficients', {'A','B'});
[fitbiolumINI,RLuINI,op] = fit(resmp_lambda_lux,mean_lux,myfit_fn,'Lower',[0,0]);
w1=(op.residuals-mean(op.residuals)).^-2;
[fitbiolum,RLu,op5] = fit(resmp_lambda_lux,mean_lux,myfit_fn,'Weight',w1,'Lower',[0,0]);
coeff_res = coeffvalues(fitbiolum);
A1=coeff_res(1);
B1=coeff_res(2);
pred_fn = A1.*biolum_ref(resmp_lambda_lux)+B1.*Bkgnd(resmp_lambda_lux);
figure(1);
plot(lambda_lux,data_lux,'*',resmp_lambda_lux,mean_lux,'o',resmp_lambda_lux,mean_Bk,'k',
resmp_lambda_lux,pred_fn,'b',resmp_lambda_lux,A1.*biolum_ref(resmp_lambda_lux));
coeff_res = coeffvalues(fitBioDK);
AD1=coeff_res(1);
BD1=coeff_res(2);
Conf_IntDK=confint(fitBioDK);
Conf_IntDnK=confint(fitBioDNK);
pred_fn2 = AD1.*biolum_ref(resmp_lambda_lux)+BD1.*Bkgnd(resmp_lambda_lux);
Pred_D_K_low=Conf_IntDK(1,1).*biolum_ref(resmp_lambda_lux)+
Conf_IntDK(1,2).*Bkgnd(resmp_lambda_lux);
Pred_D_K_high=Conf_IntDK(2,1).*biolum_ref(resmp_lambda_lux)+
Conf_IntDK(2,2).*Bkgnd(resmp_lambda_lux);
Mean_Dk=AD1.*biolum_ref(resmp_lambda_lux);
Mean_Dk_Hi=Conf_IntDK(2,1).*biolum_ref(resmp_lambda_lux);
Mean_Dk_Lo=Conf_IntDK(1,1).*biolum_ref(resmp_lambda_lux);
Err_Dk=[Mean_Dk_Hi-Mean_Dk,Mean_Dk-Mean_Dk_Lo];
figure(2)
plot(lambda_dark_KCl,data_darkK,'*',resmp_lambda_dark_KCl,
resmp_Mean_Biol_dark_KCl,'o',resmp_lambda_lux,pred_fn2,
resmp_lambda_lux,AD1.*biolum_ref(resmp_lambda_lux));
coeff_res = coeffvalues(fitBioDNK);
ADN1=coeff_res(1);
BDN1=coeff_res(2);
pred_fn3 = ADN1.*biolum_ref(resmp_lambda_lux)+BDN1.*Bkgnd(resmp_lambda_lux);
Pred_DnK_low=Conf_IntDnK(1,1).*biolum_ref(resmp_lambda_lux)+
Conf_IntDnK(1,2).*Bkgnd(resmp_lambda_lux);
Pred_DnK_high=Conf_IntDnK(2,1).*biolum_ref(resmp_lambda_lux)+
Conf_IntDnK(2,2).*Bkgnd(resmp_lambda_lux);
Mean_Dnk=ADN1.*biolum_ref(resmp_lambda_lux);
Mean_Dnk_Hi=Conf_IntDnK(2,1).*biolum_ref(resmp_lambda_lux);
Mean_Dnk_Lo=Conf_IntDnK(1,1).*biolum_ref(resmp_lambda_lux);
Err_Dnk=[Mean_Dnk_Hi-Mean_Dnk,Mean_Dnk-Mean_Dnk_Lo];
figure(4)
%
boundedline(resmp_lambda_lux,Mean_Dk,Err_Dk,'alpha')
hold on;
boundedline(resmp_lambda_lux,Mean_Dnk,Err_Dnk,'r','alpha')
hold off;
```

```
%
figure(5)
plot(resmp_lambda_lux,resmp_mean_Bk,lambda_dark_KCl,data_darknK,'*',
resmp_lambda_dark_KCl,resmp_Mean_Biol_dark_no_KCl,'o',
resmp_lambda_lux,pred_fn3,resmp_lambda_lux,ADN1.*biolum_ref(resmp_lambda_lux));
```

1.14.2 Micromanager script (*imcapture.bsh*) to instruct ANDOR iXonEM+ 897 camera to record bioluminescent and brightfield images alternatively.

```
acqName="testacq_01";
rootDirName="C:/Users";
gui.closeAllAcquisitions();
gui.clearMessageWindow();
cameraName=mmc.getCameraDevice();
numFrames=200;
gui.openAcquisition(acqName,rootDirName,numFrames,1,1);
hex=1000;
lex=6;
for (int i=0; i<numFrames; i++)
{
mmc.setProperty(cameraName, "Gain", "1000");
mmc.setExposure(hex);
gui.snapAndAddImage(acqName,(2*i+1),0,0,0);
mmc.setProperty(cameraName, "Gain", "20");
mmc.setExposure(lex);
gui.snapAndAddImage(acqName,(2*i+2),0,0,0);
}
```

1.14.3 Microcontroller program (*MicroscopeLight.ino*) for driving flash circuit

```
int sensorIn = 5; // For now set as Pin 5 of the arduino
int ledon = 7;    // Output pin to hook to the LED
int sensorRead = 0;
int i;
int time_small = 10;
int time_big = 100;
int time_wait = 20;
void setup() {
// put your setup code here, to run once:
pinMode(sensorIn, INPUT);
pinMode(ledon, OUTPUT);
pinMode(LED_BUILTIN, OUTPUT);
}
void loop() {
// put your main code here, to run repeatedly:
sensorRead = digitalRead(sensorIn);
if(sensorRead == HIGH)
    {
    for( i=0;i<(time_big/2)+1;i++)
        {
        delay(1);      // Delay of time_big/2 ms in total
        }
    sensorRead = digitalRead(sensorIn);
    if (sensorRead == HIGH)
        {
        while( digitalRead(sensorIn) == HIGH)
            {
            delay(1);
            }
        for( i=0;i<(time_wait/2);i++)
            {
            delay(1);      // Delay of time_big/2 ms in total
            }
        while( digitalRead(sensorIn) == LOW)
```

```
            {
            delayMicroseconds(100);
            }
        digitalWrite(LED_BUILTIN,HIGH);
        digitalWrite(ledon,HIGH);
        while( digitalRead(sensorIn) == HIGH)
            {
            delayMicroseconds(100);
            }
        digitalWrite(LED_BUILTIN,LOW);
        digitalWrite(ledon,LOW);
        }
    }
}
```

1.14.4 AWK program (*slicegen.awk*) for generating ImageJ macro to process movies

```
# slicegen.awk for generating ImageJ macro lum200_11stp.ijm
#do while statement
BEGIN {
#initialize a counter
x=0
for (i=1;i<=189; i++)
    {
    printf("selectWindow(\"Lum\")\n");
    printf("run(\"Z Project...\", \"start=" i" " "stop="i+10" " "projection =[Sum Slices]\")\n");
    }
}
```

1.14.5 MATLAB code (*stcfiltfun.m*) for reconstructing the in vivo voltage signals of *C. elegans* Pharyngeal muscles

```
% MATLAB code for reconstructing a representation of the ground truth signal trace
% Inputs: Ground truth and bioluminescence voltage signals: EPG_data’ and ‘blr_data’
%Output: Representation of the ground truth: nvecd
clear all;
%Read EPG data to generate stimulation trace
EPG_data=readtable(’EPG_data_zeropad_500ms’); %Digitized EPG or AP data
epgx=EPG_data.Time;
epgy=EPG_data.Voltage;
xq=0:0.001:0.5;
[epgx,index]=unique(epgx);
yq=interp1(epgx,epgy(index),xq);
epgy=3.0+yq’;
epgx=xq’;
epgt=epgx(end);
epglen=length(epgx);
%Read 100s of Bioluminescent Response
blr_data=readtable(’pic01_blr200s_serotonin’);
blrm=blr_data.BLSignal;
%blrm=(0.5+rand(5000,1)); %Random input
%blrm=bootstrp(3000,@mean,blrm); %Bootstrap sampling
reslen=length(blrm);
nc=1;
for k=1:1:reslen
randnoise=(normrnd(0.5,0.5,[epglen,1]));
epgyn=conv(epgy,randnoise);
epynlen=length(epgyn);
repgloc=randi(epynlen);
s(nc,1)=repgloc;
if repgloc < ((epglen+3)/2)
stim_trace(k,:)=[epgyn(1:epglen,1); zeros((epynlen-epglen),1)]’;
end
if repgloc > (epglen+1)/2 && repgloc < (3*epglen+1)/2
```

```
repstrt=repgloc-((epglen-1)/2+1);
repend= repstrt+epglen-1;
stim_trace(k,:)= [zeros(repstrt-1,1); epgyn(repstrt:repend,1); zeros(epynlen-repend,1)]';
end
if repgloc > (2*epynlen-epglen+1)/2
stim_trace(k,:)=[zeros(repgloc-(((epglen-1)/2)+2),1); epgyn((repgloc-1-((epglen-1)/2)):epynlen,1)]';
end
nc=nc+1;
end
for i=1:1:reslen
area=cumtrapz(stim_trace(i,:));
stim_trace(i,:)=stim_trace(i,:)/area(end);
end
stim_trace_sum(:,:)=0.0;
for k=1:1:reslen
stim_trace_sum = stim_trace_sum + stim_trace(k,:);
end
sta=stim_trace_sum/reslen;
for k=1:1:reslen
stim_dev_trace(k,:)=stim_trace(k,:)-sta;
end
stim_dev_sumsq=0.0;
stim_sumsq=0.0;
for k=1:1:reslen
ssd(k,:)=stim_dev_trace(k,:);
sst(k,:)=stim_trace(k,:);
stim_dev_sumsq = stim_dev_sumsq + blrm(k,1)*ssd(k,:)'*ssd(k,:);
stim_sumsq=stim_sumsq+sst(k,:)'*sst(k,:);
end
stc=stim_dev_sumsq/(reslen-1);
c=stim_sumsq/(reslen-1);
R=stc-c;
% Evaluate the eigen pairs
[V,D]=eig(R);
dlen=length(D(1,:));
eigval=D*ones(dlen,1);
nc= 0;
maxval=0;
for i=1:1:dlen
if imag(eigval(i,1))==0
maxvalr=real(eigval(i,1));
if maxvalr>maxval
maxval=maxvalr;
end
end
end
for ik=1:1:dlen
if nc==0 && real(eigval(ik,1))==maxval
nc = ik;
end
end
vec=V(:,nc);
%Computing Normalized vector, Integral and Differential outputs
nvec=vec/max(vec);
nvecd=diff(nvec);
```

1.15 Statistical Analysis

All experiments were performed unblinded.

1.15.1 A statistical approach for ranking the engineered proteins

We observed variability in the expression of engineered protein constructs in HEK293 cells both within a batch and between the batches. While we initially ranked the performance of different engineered protein constructs on the basis their normalized fractional luminescence $(\Delta L/L)^n$, we also observed the same outcomes from the results of statistical models. In principle, when the differential signal is sufficiently bright that it can be detected against its background, then the differential pixel value will determine the possibility of describing the morphology of the cells as observed under brightfield illumination. We define a new metric to quantify the pixel information transmission, IR after KCl challenge as the ratio of the Shannon information [36] encoded by the differential bioluminescence to the Shannon information encoded by the brightfield illumination. Mathematically, I_R is expressed as

$$I_R = 2.(H_d - H_{bf}) \tag{14.1}$$

where H_d and H_{bf} represents Shannon entropies of the pixels encoding differential bioluminescence and bright field intensities respectively.

We used 8-bit post-processed bioluminescent micrographs to evaluate Shannon entropy values using the MATLAB (R2019a) in-built function, *entropy* [15]. Table S4 lists the percentage of information transmitted carried in the differential bioluminescence for various engineered proteins. The ranking of the candidates based on I_R agrees excellently with the ranking outcomes based on the normalized fractional bioluminescence.

1.15.2 Statistical significance of cellular bioluminescence

We did not assume any particular statistical model for the analysis of our data but we found that our data did not meet the normality criterion set by Shapiro-Wilk test statistic (Significance level, $\alpha = 0.05$). However, we estimated the deviation from the normality is very small (Shapiro Wilk statistic, $W_{sw} > 0.9$ and is close to ≈ 1.0 for all the key engineered proteins) and the distribution is moderately skewed (skewness vary between -0.36 and 1.1). Wilcoxon Signed Rank test is more robust to the presence of outliers ($< 2.4\%$ as estimated by Tukey Fence, k=1.5) and a moderate deviation from the normality than the paired t-test. We, therefore, performed paired single-tailed (Left) non-parametric Wilcoxon Signed Rank test to confirm the difference in the bioluminescence of cells expressing engineered proteins after KCl addition is statistically significant. Table S5 shows the outcome of the test for different engineered proteins considered. The test compares the probability of a random bioluminescent signal at the resting state with that of its dependent signal after KCl addition. We defined our null hypothesis, H_0: Resting signal $\geq$ Depolarized signal. The alternate hypothesis, H_1: Resting signal $<$ Depolarized signal. The number of pixel counts affected after KCl addition was high enough to provide the necessary statistical power for the hypothesis test. The effect size for all the constructs was consistently large (≈ 0.87) suggesting at least 80% of the pixels describing the resting state bioluminescent signal are below the mean bioluminescent signal of the pixel after KCl addition.

1.15.3 KCl titration data

For KCl titration experiment, n=8 cells from a chosen field of view were randomly selected using a $100\mu m \times 100\mu m$ window. We evaluated an increase in the bioluminescent intensity at the chosen locations accounting for the local background signal for an incremental addition of KCl into the bath. Assuming on-off state of the voltage sensor being described as a two state model [24], the total intensity for any particular concentration was obtained as a cumulative sum of the intensity values of all the previous steps. Mean and standard error of the intensities were computed from the intensity values recorded at the chosen locations.

1.15.4 Patch clamp recordings

We reported the variability of six independent measurements taken between -60mV to 60mV at an increment of $+20$mV from a stable single cell patch. Mean and standard error of the bioluminescent intensities were evaluated using the raw data. The voltage dependent signal rise followed a typical Boltzmann model as observed in the KCl titration experiment. Shapiro Wilk normality test of the signals at off (-60mV) and on ($+60$mV) states revealed that there is a likelihood for the data to follow normal distribution (normality p-value $\approx 0.562 >$, Significance level, $\alpha = 0.05$). A paired t-test of the data set confirmed a significant difference between the mean bioluminescent intensities at the off and on states.

1.15.5 In vivo experiments

We confirmed the AMBER function in vivo based on the optical readouts characterising the voltage activities of the pharyngeal muscles and mechanosensory touch neurons. We did not consider any predetermined sample size for the statistical analysis of the in vivo recordings. We, however, reconstructed the voltage activities of pharynx (both EPG and terminal bulb action potential) from sufficient number of animals under serotonin ($n = 5$ animals) and bacterial feeding ($n = 3$ animals) conditions. We applied bootstrapping with replacement approach to increase the sample size of the recordings because both stimulated starvation and bacterial feeding conditions cause rhythmic pumping action albeit at different average rates [34].

Unlike voltage imaging of the pharynx, we did not intend to quantify the touch neuronal activities but only report qualitative assessment of varying levels of activities for different motion trajectories. Voltage imaging of mechanosensory touch neurons were obtained from several animals with different motion trajectories – burst reversal ($n = 3$ animals) and single/multiple collisions ($n = 12$ instances).

1.16 Western Blot

We estimated the molecular weights of engineered AMBER protein constructs by Western blot. We transfected 1×10^6 HEK293 cells with plasmid DNAs expressing engineered AMBER proteins and plated them into a 60mm tissue culture dish. After 48 hours post-transfection, the culture media was aspirated out and the cells were gently washed with 1mL of 1X PBS. The washed cells were then lysed by gently agitating in lysis buffer (150mM NaCl, 0.1% Triton X-100, 0.5% Sodium deoxycholate, 0.1% Sodium dodecyl sulfate, 50mM Tris-HCl, pH 8.0 with 1 Roche protease inhibitor tablet) for 30 minutes at 4^oC. The crude lysate was centrifuged at 10000g for 15 min at 4^oC to separate the soluble and insoluble fractions. Protein samples for gel electrophoresis were prepared by mixing $25\mu L$ of the soluble fraction with $25\mu L$ of Laemmli 2X sample buffer (Catalog# 161-0737; BIO-RAD) followed by denaturation by heating up to 70^oC for 5 minutes. All heated samples were loaded into individual wells of a precast protein gel (4-15% BIO-RAD Mini-PROTEAN TGX Gels; Catalog# 456-1084) and protein molecules of different molecular weights were electrophoretically separated (120 V for 1 hour not exceeding 86 mA) in a bath of running buffer (MOPS SDS, 25mM Tris base, 190mM Glycine, 0.1% SDS, pH 8.5). The protein impregnated gel was carefully removed from the cassette and placed on a 5cm × 5cm nitrocellulose membrane (Catalog#162-0112; 0.2mm; BIO-RAD) with a filter paper (Catalog# 1703965, BIO-RAD) backing submerged inside a bath of transfer buffer (25mM Tris base, 190mM Glycine, 20% methanol, pH 8.3). The gel-membrane pair sandwiched with filter paper on either side was placed in contact with an ice pack inside a Mini Trans-Blot cell (Serial# 153 BR 76868; BIO-RAD). Electrically driven ($\approx$ 90 V) wet protein transfer onto the sandwiched membrane was accomplished in a temperature regulated transfer bath. The membrane containing transferred proteins was then blocked using a blocking buffer (LI-COR Odyssey blocking buffer (PBS); Part# 927-40000) overnight at 4^oC and washed with TBST buffer (20mM Tris, 150mM NaCl, 0.1% Tween 20, pH 7.5) for 15 minutes thrice. We stained for the YPet using a primary antibody that specifically targets the epitope of most GFP variants (Monoclonal anti-GFP IgG2a raised in the mouse; Invitrogen; Catalog# A-11120). The primary antibody at 1:1000 dilution was added directly into the bath (a mixture of 7mL of TBST and 3mL of blocking buffer) with membrane immersed and was incubated at room temperature on a rocking shaker (BR2000 2D rocker; Benchmark Scientific Inc.) for 1hr. The non-specific binding of the primary antibody was removed by washing the membrane thrice for 15 minutes with 10mL of TBST at room temperature on the rocking shaker. This was immediately followed by secondary antibody treatment (IRDyeÒ 680LT Goat anti-Mouse IgG; LI-COR; Catalog# 926-68020) at 1:10000 dilution for 1hr at room temperature and subsequently washing with TBST buffer thrice. The secondary antibody is sensitive to fluorescent emission at 700 nm, that is detected using a membrane-imaging system (Odyssey CLx, LI-COR). Protein bands emitting fluorescent signals were then processed using Image Studio software (version 5.2).

Table S1: Biochemical reactions performed to create plasmids for expressing engineered proteins in HEK293 cells and *C. elegans*

Template	Reagents	Forward (F) and Reverse (R) primers	Reactions	Descriptive Notes	Modified plasmids and DNA fragments
VSFP2.1	Quick Change Site-Directed Mutagenesis (QCSDM); (Agilent; Catalog # 210518)	F: 5’-gtaccgagctcggagccactagtccagtg-3’ R: 5’-cactggactagtggctccgagctcggtac-3	Substitution Mutation	BamHI site flanking Cerulean domain.	NotI-VSFP2.1-BamHI
pCMVlux		F: 5’-ccccctgatcccccaccggatcccatatggtatttcttgatgttgtcgt-3’ R: 5’-acgacaacatcaagaaataccatatgggatccggtgggggatcaggggg-3’	Substitution Mutation	BamHI site flanking luxB	luxB-BamHI
luxB-BamHI		F: 5’-ctggtagaagttccgcagcacgcggccgctctcgctcaggtcgtgggagc-3’ R: 5’-gctcccacgacctgagcgagagcggccgcgtgctgcggaacttctaccag-3’	Substitution Mutation	Creating NotI site 270bp upfront of luxA inside luxD.	270nt_luxA-luxB-BamHI
NotI-VSFP2.1-BamHI and 270nt_luxA-luxB-BamHI	BamHI-HF (NEB, R3136S), NotI-HF(NEB, R3189S), and 10X CutSmart Buffer	None	Double digestion at BamHI and NotI sites	Double stranded (ds) vector, and insert fragments	VSFP2.1 vector backbone, and the 270nt_luxA-luxB insert
VSFP vector backbone and 270nt_luxA-luxB insert	T4 DNA ligase, and 10X ligation buffer (NEB, M0202S)	None	Ligation	Ligation of VSFP vector backbone, and 270nt_luxA-luxB insert	VSD-270nt_luxA-luxB-YFP
VSD-270nt_luxA-luxB-YFP	QCSDM (Agilent; Catalog # 210518)	F: 5’-cgtcgatgcggccgcatgaagttcggcaac-3’ R: 5’-gttgccgaacttcatgcggccgcatcgacg-3’	Deletion Mutation	Delete the additional 270bp flanking the 5’ of luxAB	VL-YFP
VL-YFP	Quick Change Multi Site-Directed Mutagenesis (QCMSDM); (Agilent; Catalog # 200514)	5’-tctgcttgtcggcagtgatatagacgttgtggctgttgta-3’ 5’-cctcgtgaccaccttaggctacggcct-3’ 5’-aggccgtagcctaaggtggtcacgagg-3’ 5’-tacaacagccacaacgtctatatcactgccgacaagcaga-3’	Substitution at multiple sites	Modification of Citrine to YFP3	VL-YFP3
VL-YFP3		5’-tgtggcggatcttgaagttagccttgatgccgttcttctg-3’ 5’-cggcgagctgcacaccgccgtcctcgatg-3’ 5’-ctaccagtccgccctgttcaaagaccccaacgag-3’	Substitution at multiple sites	Modification of YFP3 to YPet	VL-Y
VL-Y		5’-ccggcatcagcaacgtctgctgcggcttt-3’ 5’-aaagccgcagcagacgttgctgatgccgg-3’ 5’-ccttgatgctgtcgtagtccacgctggtgat-3’ 5’-atgctggcgacaatctcgtccacggtgccg-3’ 5’-ctcgttgtcggcttctatgtagccctcggtc-3’	Substitution at multiple sites	Modification of luxA-luxB to eluxA-eluxB	V-EA-EB-Y
V-EA-EB-Y	QCSDM	F: 5’-atagcgctgggtgctgcgttttcttcgacatctcc-3’ R: 5’-ggagatgtcgaagaaaacgcagcacccagcgctat-3’	Substitution Mutation	Mutating T2A prolines to alanines to fuse eluxA and eluxB	VE-Y
VE-Y		F: 5’-ctagtccagtgtggtgggatcccttgtacagctcgtcc-3’ R: 5’-ggacgagctgtacaagggatcccaccacactggactag-3’	Substitution mutation	Introducing BamHI site at 3’ end of YPet	VE-Y-BamHI
VE-Y-BamHI	BamHI-HF (NEB, R3136S), and 10X CutSmart Buffer	None	Double digestion at two BamHI sites	Double stranded vector, and insert fragments	BamHI-BB-VE-BamHI, and BamHI-Y-BamHI fragments
BamHI-BB-VE-BamHI	T4 DNA ligase, and 10X ligation buffer (NEB, M0202S)	None	Ligation	Self ligation of the large fragment	VE
VE	QCSDM	F: 5’-ctcggagccactagtccagtgtggcggccgcacatatggtatttcttgatgttgtc-3’ R: 5’-gacaacatcaagaaataccatatgtgcggccgccacactggactagtggctccgag-3’	Substitution Mutation	Converting BamHI to NotI	VE-NotI
VE-NotI		F: 5’-gcaggaagttgccgaacttcatgtgggatcctcgacgcttgttctgtgatattg-3’ R: 5’-caatatcacagaacaagcgtcgaggatcccacatgaagttcggcaacttcctgc-3’	Substitution Mutation	Converting 5’ NotI flanking eluxAB to BamHI	V-BamHI-eluxAB-NotI
V-BamHI-eluxAB-NotI	BamHI-HF (NEB, R3136S), and 10X CutSmart Buffer	None	Digestion at the BamHI site	dsDNA fragment	BamHI-eluxAB-V-BamHI
BamHI-eluxAB-V-BamHI, and BamHI-Y-BamHI fragments	T4 DNA ligase, and 10X ligation buffer (NEB, M0202S)	None	Ligation	Ligation of small and large dsDNAs	VY-E
pCMVlux	QCSDM	F: 5’-gtaaccccggtcctaatttaaatcgcgggtggatg-3’ R: 5’-catccacccgcgatttaaattaggaccggggttac-3’	Deletion Mutation	Delete luxA and luxB domains	luxCDE-FRP
luxCDE-FRP	QCSDM	F: 5’-gggcctggccaagagataagctagcagctcgctga-3’ R: 5’-ggaggagaatcccggccctgctagcatgaacaacaccatcgaga-3’	Substitution Mutation	FRP domain with flanking BmtI sites	luxCDE-BmtI-FRP-BmtI
luxCDE-BmtI-FRP-BmtI	BmtI-HF (NEB, R3658S), and 10X CutSmart Buffer	None	Digestion at the BmtI sites	dsDNA fragment	BmtI-FRP-BmtI; BmtI-luxCDE-BmtI
BmtI-luxCDE-BmtI	T4 DNA ligase, and 10X ligation buffer (NEB, M0202S)	None	Ligation	Self ligation of the large fragment	luxCDE
VY-E	BmtI-HF (NEB, R3658S), and 10X CutSmart Buffer	None	Digestion at the BmtI sites	dsDNA large fragment	BmtI-VY-E-BmtI
VE-Y	BmtI-HF (NEB, R3658S), and 10X CutSmart Buffer	None	Digestion at the BmtI sites	dsDNA large fragment	BmtI-VE-Y-BmtI
BmtI-VY-E-BmtI, and BmtI-FRP-BmtI	T4 DNA ligase, and 10X ligation buffer (NEB, M0202S)	None	Ligation	Ligation of the vector, and insert fragments	FV-Y-E
BmtI-VE-Y-BmtI, and BmtI-FRP-BmtI	T4 DNA ligase, and 10X ligation buffer (NEB, M0202S)	None	Ligation	Ligation of the vector, and insert fragments	FV-E-Y
pCMVlux	QCSDM	F: 5’-atagcgctgggtgctgcgttttcttcgacatctcc-3’ R: 5’-ggagatgtcgaagaaaacgcagcacccagcgctat-3’	Substitution Mutation	Converting T2A between luxA, and luxB into a fusion linker	luxAB
MBP-rTRPV1	Phusion HF DNA polymerase (NEB; M0530L), and DpnI (NEB, R0176S)	F: 5’-ttaaacttaagcttggtaccgaacaacgggctagct-3’ R: 5’-gatatctgcagaattcttatttctcccctgggaccatggaa-3’	PCR amplification and DpnI treatment	Temperature gradient PCR with Tm between 66-72C	Amplified rTRPV1 gene
pCDNA3.1(+)	EcoRI-HF (NEB; R3101S), KpnI-HF (NEB; R3142L), and 10X CutSmart Buffer	None	Double Digestion	pCDNA3.1(+) vector backbone with flanking restriction sites	KpnI-pCDNA3.1-EcoRI
Amplified rTRPV1 and KpnI-pCDNA3.1-EcoRI	T4 DNA ligase, and 10X ligation buffer (NEB, M0202S)	None	Ligation	Ligation of vector and insert	pCDNA3.1-rTRPV1
FV-E-Y, and the synthetic Dark fragment	In-Fusion enzyme mix (TaKaRa Bio Inc; Catalog # 639649)	None	Ligation	Ligation of vector, and insert fragments	FV-E-Dark
L3691	EcoRI-HF (NEB; R3101S), KpnI-HF (NEB; R3142L), and 10X CutSmart Buffer	None	Ligation	dsDNA large fragment	KpnI-L3691-EcoRI
FV-E-Y	Phusion HF DNA polymerase (NEB; M0530L), and DpnI (NEB, R0176S)	F: 5’-tagtgagtcgtattggtaccatgaacaacaccatcgagac-3’ R: 5’-gccggctagcgaattccttgtacagctcgtccat-3’	PCR amplification and DpnI treatment	Temperature gradient PCR with Tm between 66-72C; 3%DMSO	Amplified FV-E-Y gene fragment
Amplified FV-E-Y, and KpnI-L3691-EcoRI	In-Fusion enzyme mix	None	Ligation	Ligation of the vector, and insert fragments	mec7-Btp
luxCDE	Phusion HF DNA polymerase, and DpnI	F: 5’-tagtgagtcgtattggtaccatgggcaccaagaaga-3’ R: 5’-ccggctagcgaattctcagcgagcttctagagggc-3’	PCR amplification of cDNA, and DpnI treatment	Temperature gradient PCR with Tm ranging 66-72C; +0.5mM $MgCl_2$	Amplified luxCDE gene
Amplified luxCDE, and KpnI-L3691-EcoRI	In-Fusion enzyme mix	None	Ligation	Ligation of the vector, and insert fragments	mec7-Bts
mec7-Btp and L3790	SphI-HF (NEB, R3182S), ClaI (NEB; R0197S), and 10X CutSmart Buffer	None	Restriction digestion	Digestion and purification of the vector and insert fragments	mec7-Btp backbone, and SphI-myo-2-ClaI insert
mec7-Btp backbone, and SphI-myo-2-ClaI	T4 DNA ligase, and 10X ligation buffer	None	Ligation	Ligation of the vector, and insert fragments	myo2-Btp
mec7-Bts	AscI (NEB, R0558S), BamHI-HF (NEB, R3658S), and 10X CutSmart Buffer	None	Restriction digestion	Digestion and purification of the vector fragment	mec7-Bts backbone
mec7-Bts backbone, and the Synthetic myo-2 promoter	In-Fusion enzyme mix	None	Ligation	Ligation of the vector, and insert fragments	myo2-Bts

Table S2: Fitting constants for the bioluminescent spectra of AMBER and FV-E-Dark evaluated by MATLAB programming using weighted-residual least square approach. Reported constants under different conditions include 95% confidence interval.

Engineered Proteins	**Condition**	**Fitting Constants**		
		A	**B**	**C**
AMBER	Resting	0.0595 ± 0.0106	1.103 ± 0.033	0.0281 ± 0.0130
	Depolarized	0.1931 ± 0.0161	0.9793 ± 0.0248	0.1136 ± 0.0440
FV-E-Dark	Resting	0.0676 ± 0.0088	0.9747 ± 0.0157	-
	Depolarized	0.1133 ± 0.0035	1.065 ± 0.006	-

Table S3: Measured distances (in Å) between the centre of mass of the amino acid residues at the interface of α and β subunits of vh-luxAB (PDBID: 3FGC) in the FMN unbound/bound states. Majority of these residues are hydrophobic and are shielded from the solvent environment. Proximity of a residue with its neighbours was evaluated applying a cut-off distance of 7.5 Å (distance between αPHE272 and βTYR151).

FMN Unbound			**FMN bound**		
α subunit residues	β subunit residues	Distance (Å)	α subunit residues	β subunit residues	Distance (Å)
17	161	4.7	17	161	4.7
17	159	5.3	21	95	4.2
21	95	3.9	21	160	4.0
21	160	4.3	24	96	5.5
24	96	5.6	45	88	5.8
45	88	5.9	51	159	5.1
51	159	5.2	54	88	4.9
54	88	4.9	54	89	3.5
54	89	3.4	54	92	5.5
54	92	5.4	61	63	6.5
61	96	4.8	61	96	4.6
82	117	5.6	63	61	6.8
85	117	6	82	117	5.6
95	18	5.2	85	117	5.8
96	61	4.5	85	81	6.1
96	25	4.8	88	45	5.9
153	116	5.3	95	18	5.1
154	116	5.2	96	61	4.3
261	154	4.2	96	25	4.8
266	154	4.9	115	153	5.9
266	147	4.9	115	154	4.8
272	119	5.5	117	85	5.0
272	151	7.3	117	82	5.0
			153	116	5.2
			154	116	5.4
			157	46	7.0
			159	45	7.8
			159	46	7.1
			159	48	7.1
			261	154	3.8
			265	147	6.0
			270	150	5.8
			270	120	5.4
			272	118	6.8
			272	119	5.2
			272	151	7.2

Table S4: Information entropy ratio, I_R of different engineered protein constructs.

Constructs	**Substrate Expressed**	**% Information Transmitted**
AMBER	Yes	85.40
FV-E-Dark	Yes	73.20
VE-Y	Yes	40.25
VY-E	Yes	35.15
VY-E	No	28.73
VE-Y	No	28.20
FV-Y-E	Yes	19.25
V-E	No	9.7
Untransfected	-	0.56

Table S5: Statistical analysis of the bioluminescent signals of HEK293 cells expressing engineered proteins

Wilcoxon signed-Rank Test

Two dependent samples, non-parametric paired test

Tails	Left (H_1: Resting <Depolarized)
Expected difference, μ_0	0
Method	Automatic
Significance level, α	0.05
Statistical Outliers	Included
Continuity Correction	TRUE
Null hypothesis: H_0	Resting >= Depolarized
Alternate hypothesis: H_1	Resting <Depolarized
Test statistic, Z	$(-\mu+C_{con})/s$
Outlier detection	Tukey Fence, k= 1.5

Protein Constructs	**Pixel count**	**Mean Signal**	**Signal Std. Dev.**	**Median Signal**	**Skewness**	**Normality**	**Outliers**		**Total Rank**			**Test Result**	
	n	X	S	M	sk	N	count	%	W_+	p-val	Z		W_{SW}
FRP-VSD-eluxAB-YPet +S	1872	819.95	614.52	665.50	1.12	0.00	44	2.35	1753128	0	-37.475	Reject H_0	0.91
VSD-eluxAB-YPet+S	1497	441.67	329.63	368.00	1.02	0.00	33	2.22	1121253	0	-33.513	Reject H_0	0.9252
VSD-eluxAB-YPet	158	184.61	126.37	175.50	0.44	5.48×10^{-5}	0	0	12561	0	-10.902	Reject H_0	0.9549
FRP-VSD-YPet-eluxAB +S	629	133.21	90.17	120.00	0.70	4.5×10^{-13}	15	2.38	198135	0	-21.729	Reject H_0	0.95
VSD-YPet-eluxAB+S	764	267.40	164.93	247.00	0.68	2.56×10^{-13}	7	0.92	292230	0	-23.945	Reject H_0	0.9613
VSD-YPet-eluxAB	2036	103.09	77.41	86.00	1.03	0.00	38	1.87	2073666	0	-39.082	Reject H_0	0.9242
VSD-eluxAB +S	42	84.26	73.02	47.50	0.91	2×10^{-5}	0	0	903	8.45×10^{-9}	-5.641	Reject H_0	0.8295
VSD-eluxAB+eGFP+S	1821	528.93	323.79	488.00	0.71	0.00	27	1.48	1658931	0	-36.961	Reject H_0	0.9641
Dark+S	55	415.89	95.93	427.00	-0.36	0.23	0	0	1540	5.67×10^{-11}	-6.448	Reject H_0	0.9723

Signal is defined as the difference between the pixel intensities of the cells after and before KCl treatment

$W_+ = \Sigma R_i$, where R_i is the rank of the signal of the i^{th} pixel

Standard effect size, $Z/n^{0.5} \approx 0.87$; Common language effect size= 0.0

Continuity factor, C_{con}= 0.5

W_{SW} is the Shapiro-Wilk Test statistic

Supporting Figure S1

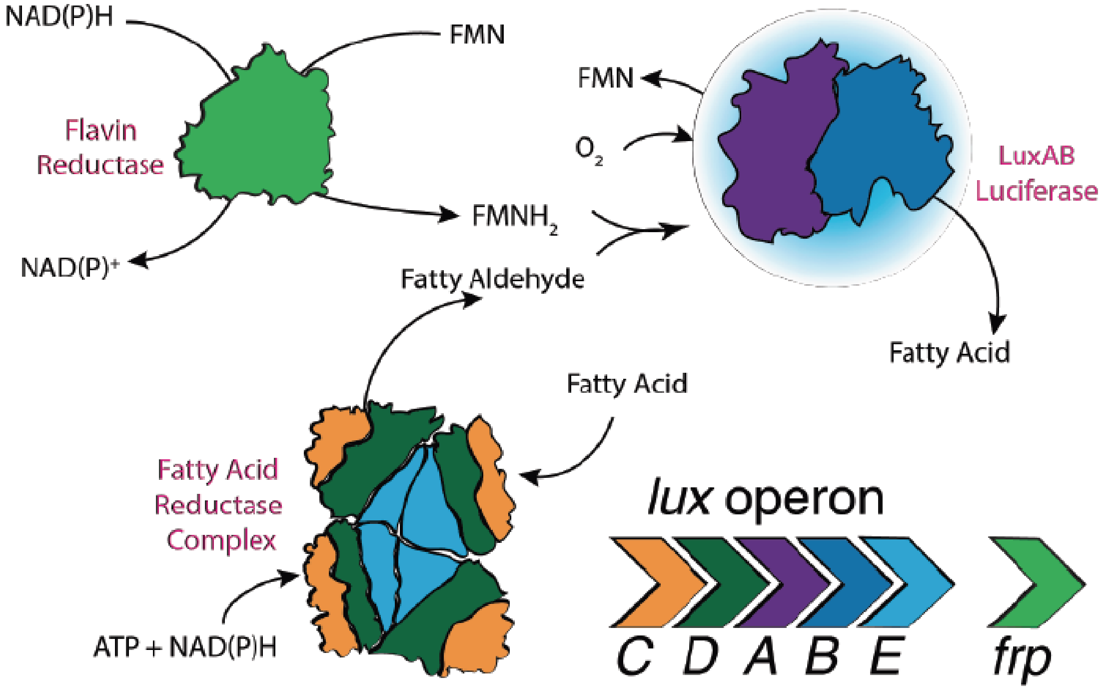

Figure S1: **Molecular mechanisms of genetically encoded bacterial bioluminescence**. Light reaction is catalyzed by the luciferase molecule, luxAB. The reactants of the light reaction are reduced flavin ($FMNH_2$), Fatty aldehyde (Myristyl aldehyde, also known as tetradecanal, a 14-carbon chain aldehyde) and molecular oxygen (O_2). $FMNH_2$ is produced by the FRP using NAD(P)H pathway. Myristyl aldehyde is produced by Fatty Acid Reductase (FAR) complex consuming ATP molecules. FAR complex comprise a set of three enzymes - synthase, reductase and transferase and these are encoded genetically in the *luxCDE* genes. luxAB oxidize $FMNH_2$ and Myristyl aldehyde to FMN and Myristic acid emitting a blue photon ($\lambda_{\max} \approx 490$ nm) as a byproduct. Both FMN and Myristic acid are recycled back as $FMNH_2$ and Myristyl aldehyde endogenously. luxAB is also known to catalyze exogenously supplied decanal (a 10-carbon chain aldehyde) emitting a blue-shifted photon in vitro but decanal is toxic to cells at high concentration ($> 0.5\%$). Steady-state concentration of Myristyl aldehyde is sufficiently high without affecting cell viability thereby making $FMNH_2$ as the rate limiting of biophoton emission.

Supporting Figure S2

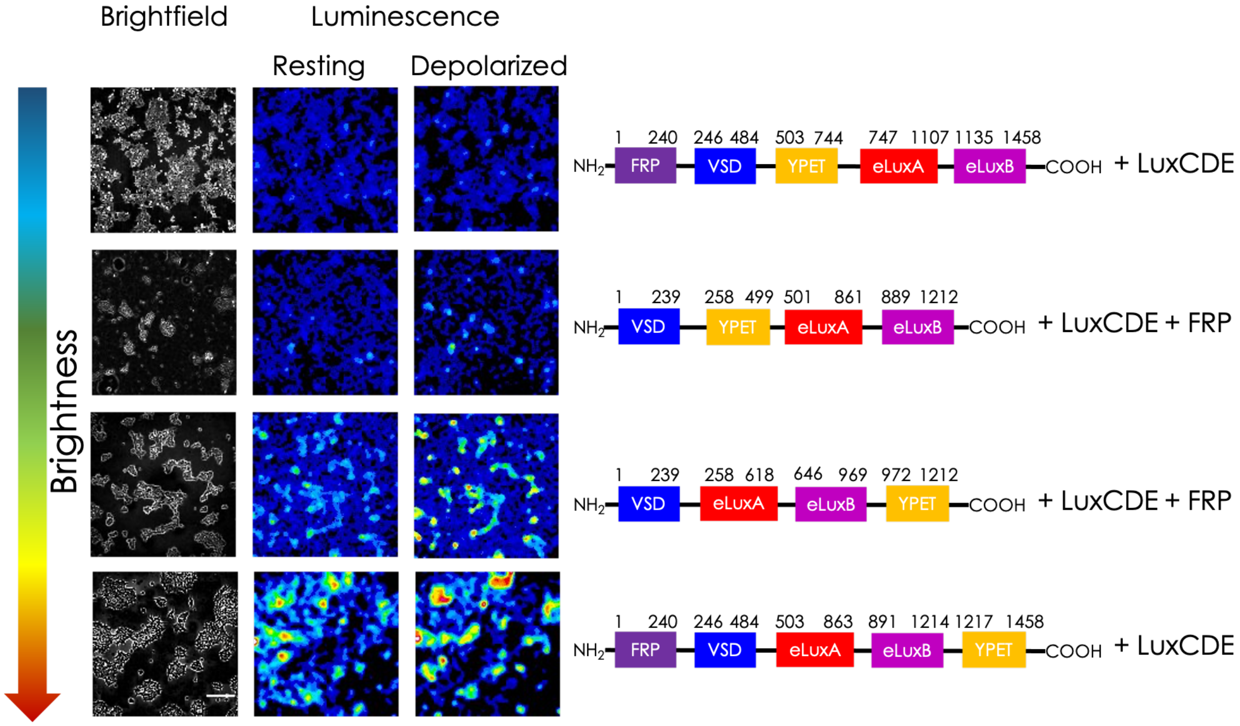

Figure S2: **Bioluminescent voltage signals of various engineered protein constructs expressed in HEK293 cells**.FV-E-Y is the brightest of all the candidates. FV-Y-E performed the worst among all the engineered candidates. See the SI Section 14 for statistical analyses of all the engineered proteins. Color coded intensity values are in the arbitrary units (a.u). The scale bar length is 200μm.

Supporting Figure S3

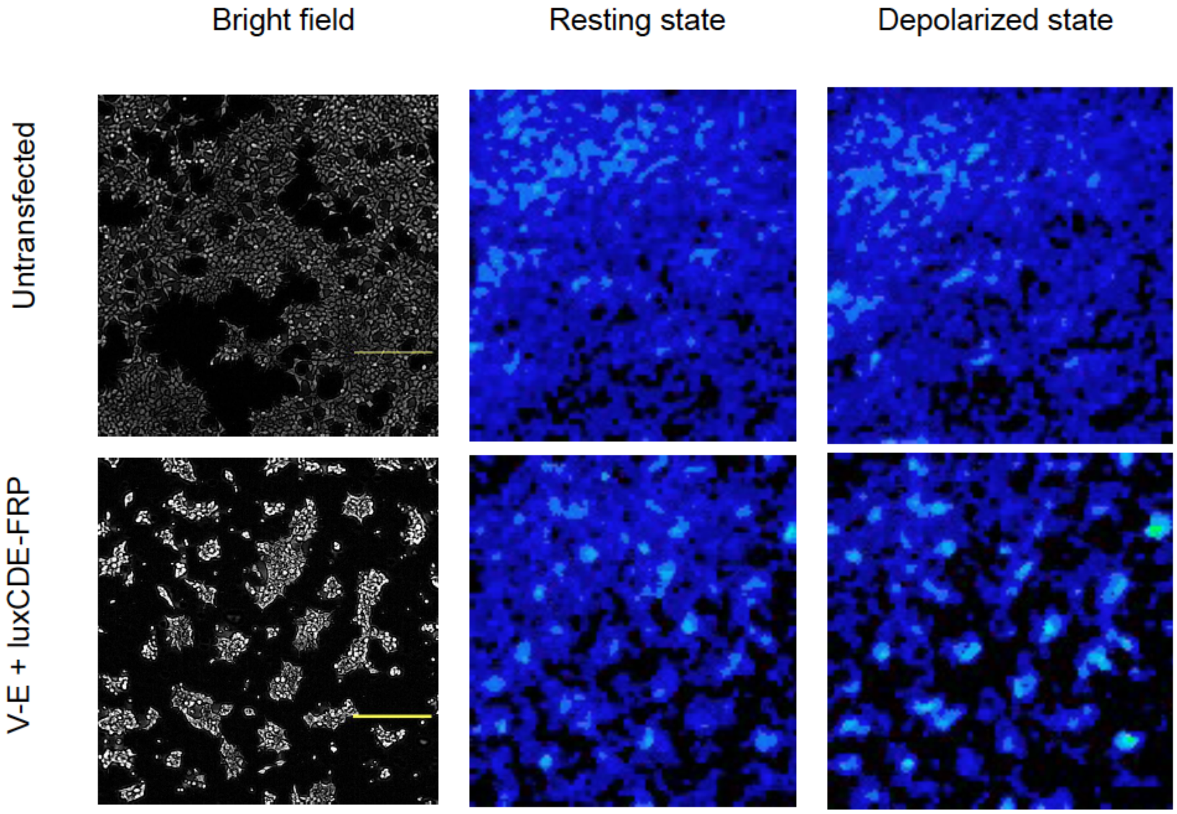

Figure S3: **Bioluminecent voltage signal is not efficiently modulated when the YPet domain is absent**.(Top) Background light emission from the untransfected HEK293 cells show negligible intensity change after KCl challenge. (Bottom) Light reaction catalyzed by V-E co-expressed with its substrate producing protein complex did not show efficient modulation after KCl addition.The scale bar length is 250μm.

Supporting Figure S4

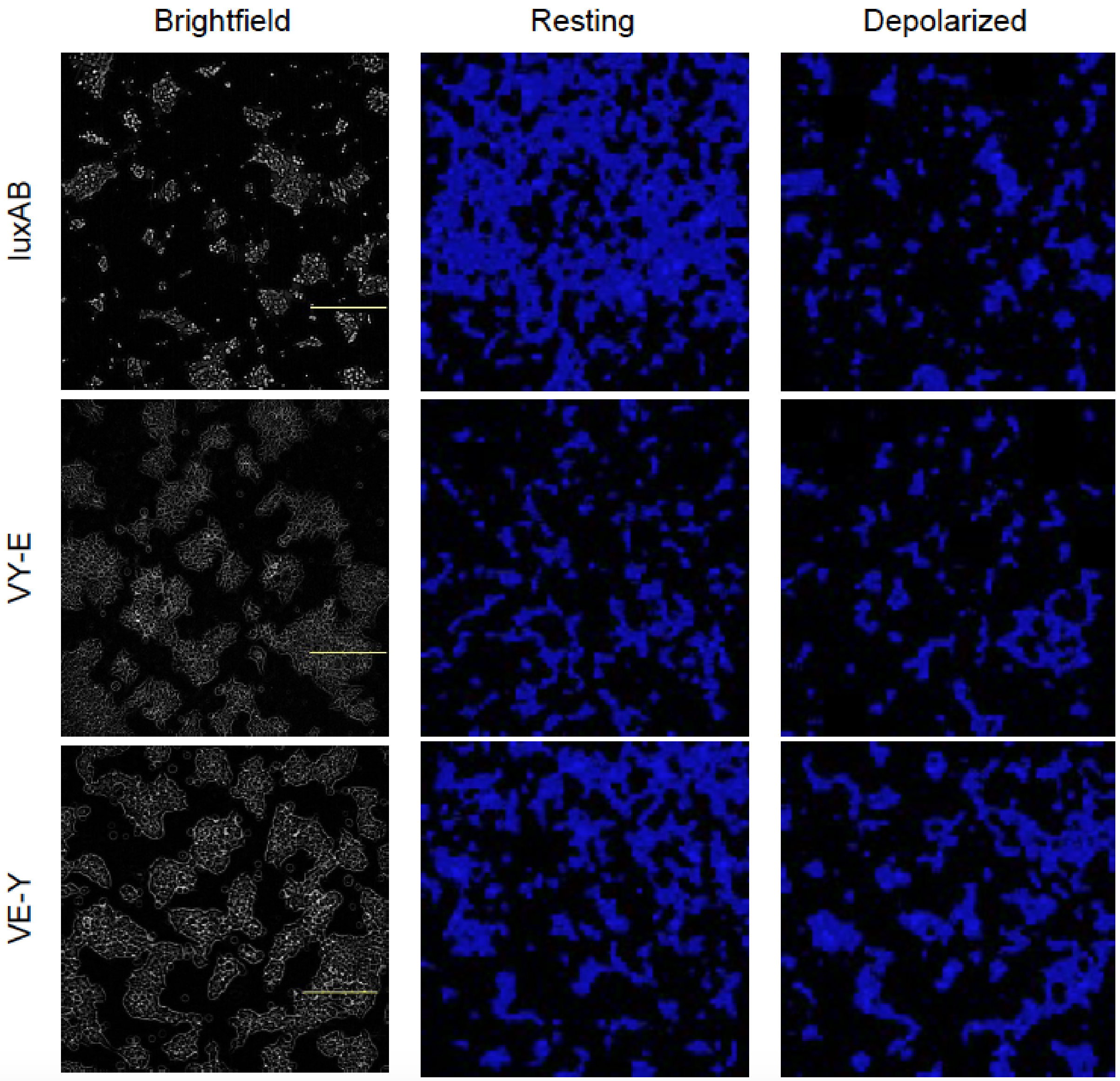

Figure S4: **Bioluminescent voltage signals due to endogenous substrate protein complex is very weak**.Signals produced were 10 times smaller than that of when substrate producing proteins were over-expressed. (Top) Cytosolic expression of *lux* operon (fused luxAB) produced a weak signal requiring 30s integration time for a brightness comparable to other membrane targeted constructs (Middle and Bottom) imaged with 10 sec integration time. The scale bar length is 250μm.

Supporting Figure S5

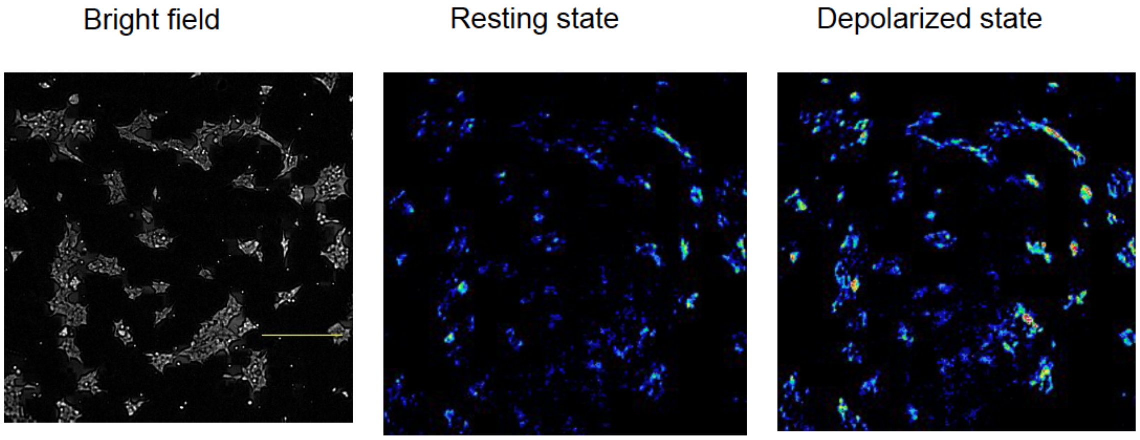

Figure S5: **Increase in the endogenous NADH fluorescence of HEK293 cells expressing AMBER after KCl addition.** NADH has a maximum fluorescent emission at $\lambda_{\max}\approx$ 440 nm (free) and $\lambda_{\max}\approx$ 462 nm (protein bound) when excited between 330-380 nm. Images shown were obtained using a DAPI filter (Ex: 350 nm and Em: 460 nm). Fluorescent signals recorded does not discriminate between the free and bound NADH signals but indicates an increase in the intensity of the multiplexed signal after KCl addition. The scale bar length is 250μm.

Supporting Figure S6

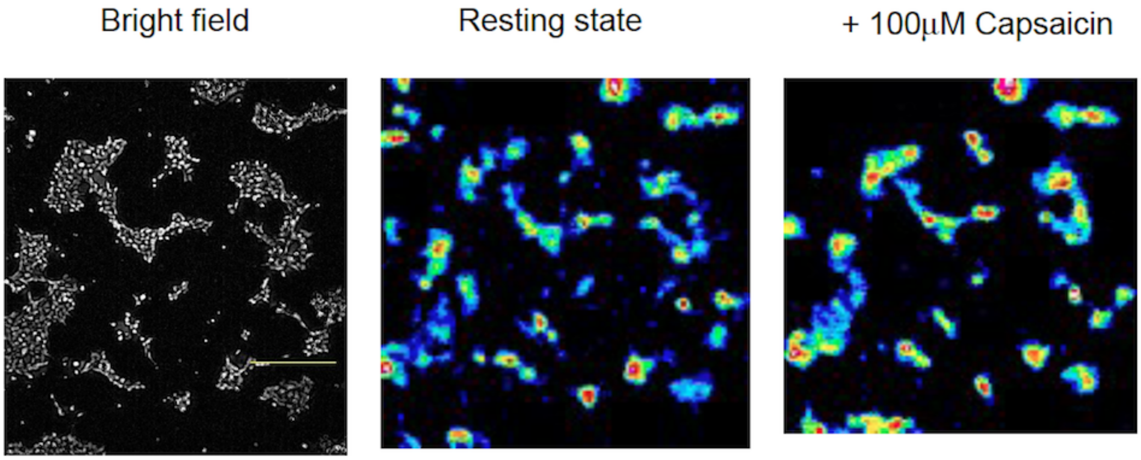

Figure S6: **Bioluminescence of HEK293 cells co-expressing AMBER and rTRPV1 after addition of Capsaicin.** Low solubility of Capsaicin necessitates a low assay volume (about 400μL) at 100μM final concentration to achieve rapid equilibration at the room temperature. An increase in the bioluminescence after activation of rTRPV1 with Capsaicin is evident although the differential signal is comparatively smaller than that observed in KCl depolarization. The length of the scale bar is 250μm

Supporting Figure S7

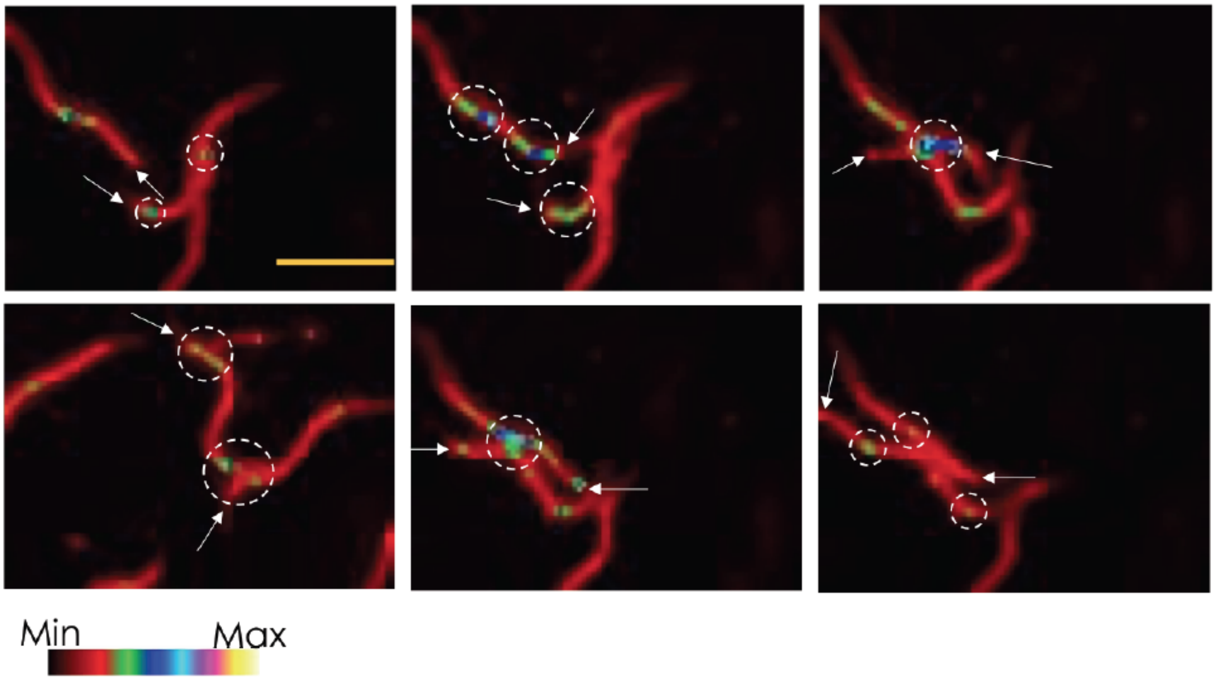

Figure S7: **Snapshots of varying levels of activity of the touch neurons in a population of worms during collision.** Touch neurons is known to respond to differential forces. Collision between animals can exert differential forces due to momentum transfer. White arrows indicate anterior end of the animals. The scale bar length is 500μm.

Supporting Figure S8

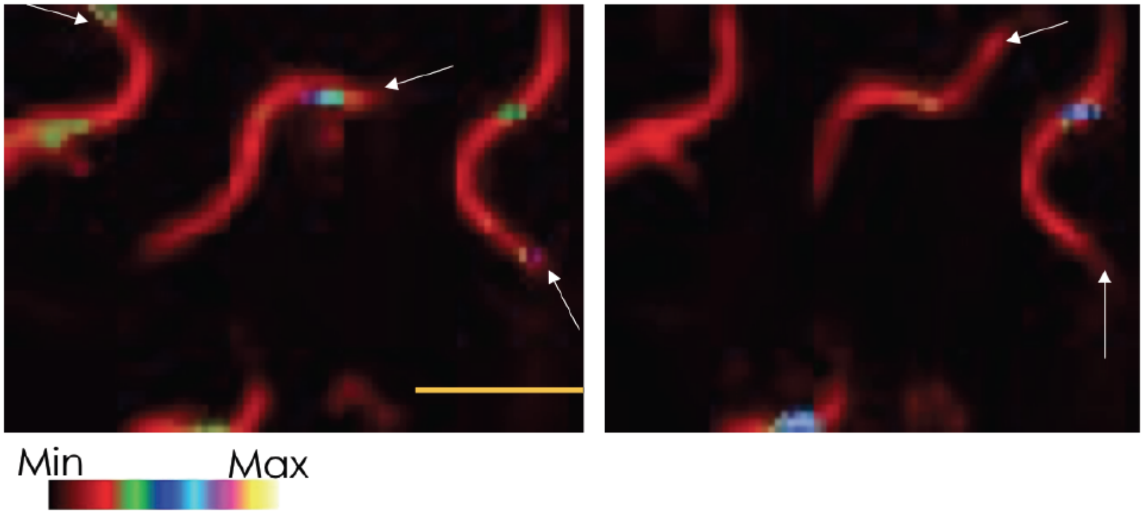

Figure S8: **Bioluminescent voltage imaging of multiple freely moving animals.** Snapshots of varying levels of activity of the touch neurons recorded from multiple animals in a single field of view. White arrows indicate anterior end of the animals. The scale bar length is 500μm.

Supporting Figure S9

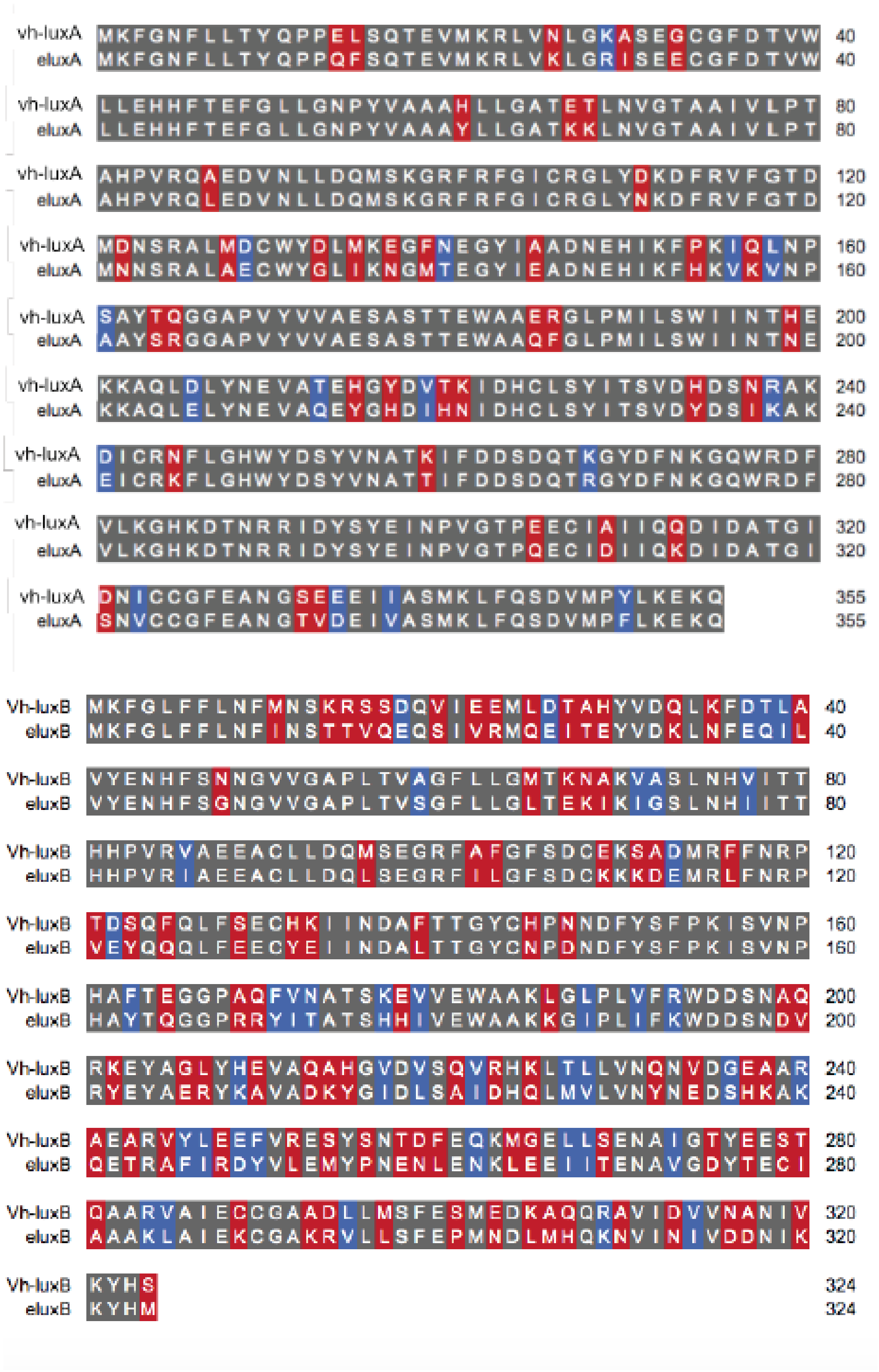

```
vh-luxA MKFGNFLLTYQPPELSQTEVMKRLVNLGKASEGCGFDTVW 40
  eluxA MKFGNFLLTYQPPQFSQTEVMKRLVKLGRISEECGFDTVW 40

vh-luxA LLEHHFTEFGLLGNPYVAAAHLLGATETLNVGTAAIVLPT 80
  eluxA LLEHHFTEFGLLGNPYVAAAYLLGATKKLNVGTAAIVLPT 80

vh-luxA AHPVRQAEDVNLLDQMSKGRFRFGICRGLYDKDFRVFGTD 120
  eluxA AHPVRQLEDVNLLDQMSKGRFRFGICRGLYNKDFRVFGTD 120

vh-luxA MDNSRALMDCWYDLMKEGFNEGYIAADNEHIKFPKIQLNP 160
  eluxA MNNSRALAECWYGLIKNGMTEGYIEADNEHIKFHKVKVNP 160

vh-luxA SAYTQGGAPVYVVAESASTTEWAAERGLPMILSWIINTHE 200
  eluxA AAYSRGGAPVYVVAESASTTEWAAQFGLPMILSWIINTNE 200

vh-luxA KKAQLDLYNEVATEHGYDVTKIDHCLSYITSVDHDSNRAK 240
  eluxA KKAQLELYNEVAQEYGHDIHNIDHCLSYITSVDYDSIKAK 240

vh-luxA DICRNFLGHWYDSYVNATKIFDDSDQTKGYDFNKGQWRDF 280
  eluxA EICRKFLGHWYDSYVNATTIFDDSDQTRGYDFNKGQWRDF 280

vh-luxA VLKGHKDTNRRIDYSYEINPVGTPEECIAIIQQDIDATGI 320
  eluxA VLKGHKDTNRRIDYSYEINPVGTPQECIDIIQKDIDATGI 320

vh-luxA DNICCGFEANGSEEEIIASMKLFQSDVMPYLKEKQ      355
  eluxA SNVCCGFEANGTVDEIVASMKLFQSDVMPFLKEKQ      355

Vh-luxB MKFGLFFLNFMNSKRSSDQVIEEMLDTAHYVDQLKFDTLA 40
  eluxB MKFGLFFLNFINSTTVQEQSIVRMQEITEYVDKLNFEQIL 40

Vh-luxB VYENHFSNNGVVGAPLTVAGFLLGMTKNAKVASLNHVITT 80
  eluxB VYENHFSGNGVVGAPLTVSGFLLGLTEKIKIGSLNHIITT 80

Vh-luxB HHPVRVAEEACLLDQMSEGRFAFGFSDCEKSADMRFFNRP 120
  eluxB HHPVRIAEEACLLDQLSEGRFILGFSDCKKKDEMRLFNRP 120

Vh-luxB TDSQFQLFSECHKIINDAFTTGYCHPNNDFYSFPKISVNP 160
  eluxB VEYQQQLFEECYEIINDALTTGYCNPDNDFYSFPKISVNP 160

Vh-luxB HAFTEGGPAQFVNATSKEVVEWAAKLGLPLVFRWDDSNAQ 200
  eluxB HAYTQGGPRRYITATSHHIVEWAAKKGIPLIFKWDDSNDV 200

Vh-luxB RKEYAGLYHEVAQAHGVDVSQVRHKLTLLVNQNVDGEAAR 240
  eluxB RYEYAERYKAVADKYGIDLSAIDHQLMVLVNYNEDSHKAK 240

Vh-luxB AEARVYLEEFVRESYSNTDFEQKMGELLSENAIGTYEEST 280
  eluxB QETRAFIRDYVLEMYPNENLENKLEEIITENAVGDYTECI 280

Vh-luxB QAARVAIECCGAADLLMSFESMEDKAQQRAVIDVVNANIV 320
  eluxB AAAKLAIEKCGAKRVLLSFEPMNDLMHQKNVINIVDDNIK 320

Vh-luxB KYHS                                     324
  eluxB KYHM                                     324
```

Figure S9: **Comparison between vh-luxAB and eluxAB protein sequences.** Unchanged residues were highlighted in grey color while residues with similar and dissimilar properties were highlighted in blue and red respectively. Majority of the eluxA sequence is unchanged (about 93% including the positives). In particular, residues defining the FMN pocket geometry and those forming the hydrophobic contact at the interface between subunits were fully conserved.

Supporting Figure S10

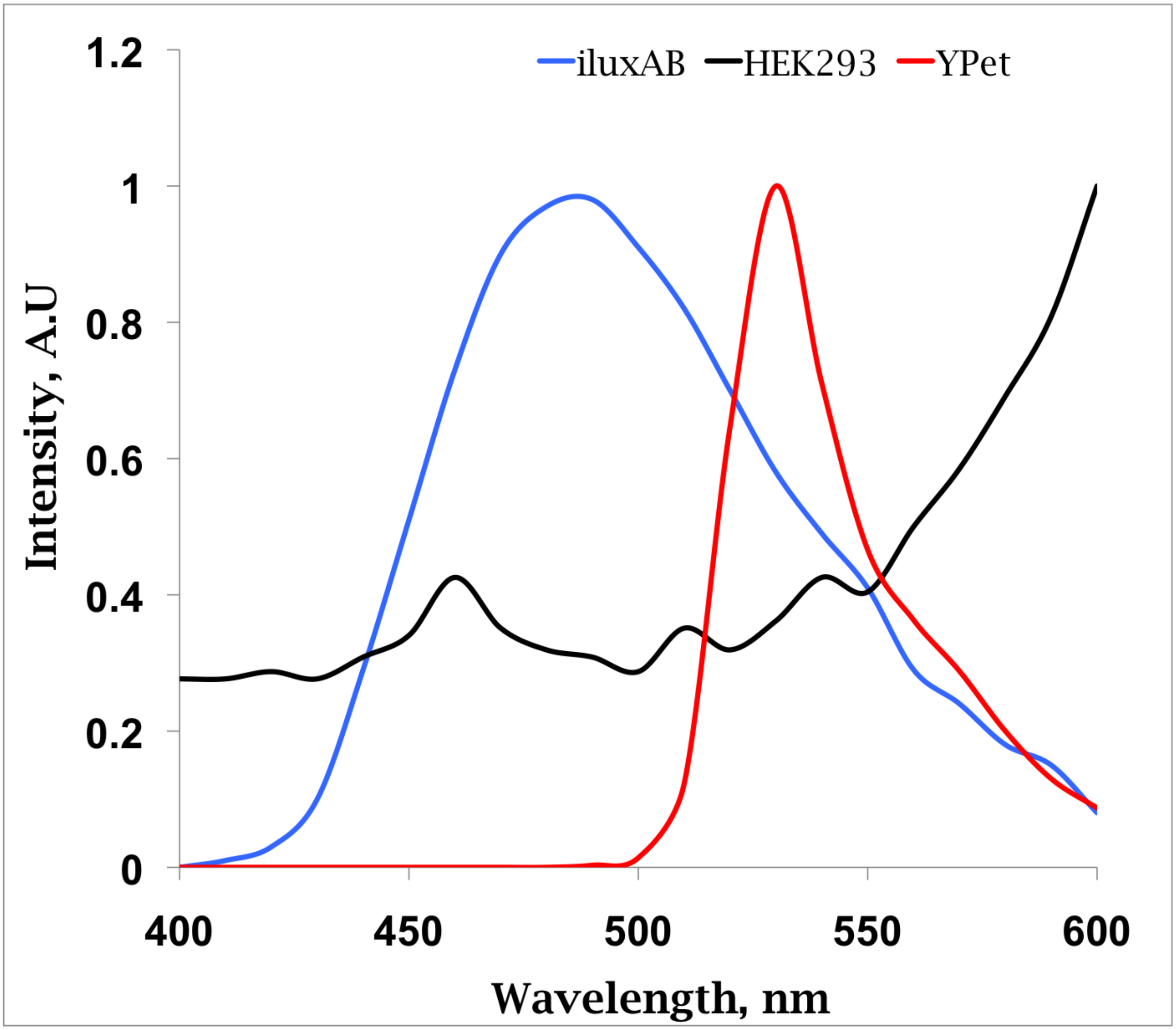

Figure S10: **Spectral components of the bioluminescent engineered voltage sensors.** Using WebplotDigitizer tool[31], bioluminescent emission spectrum of the iluxAB[16] and fluorescent emission spectrum of the YPet[23] were digitized to model the non-linear spectral curve fits of the AMBER and FV-E-Dark. Background emission of HEK293 cells were obtained experimentally as the median photon counts of n= 8 individual samples.

Supporting Figure S11

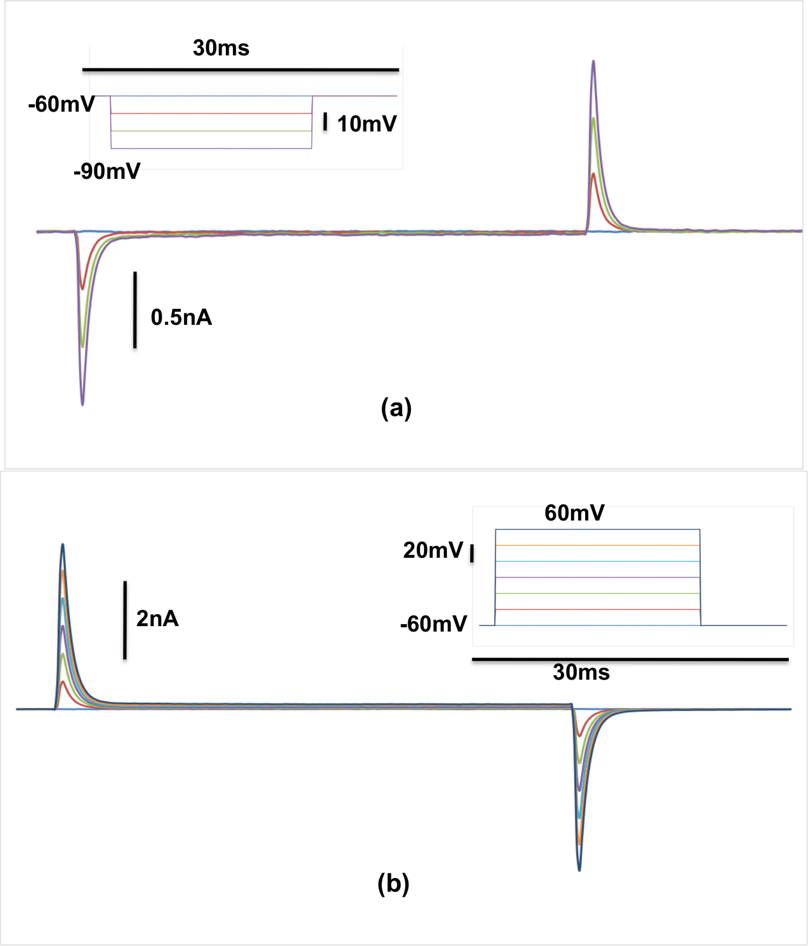

Figure S11: **Voltage-Current characteristics of a HEK293 cell expressing AMBER under whole cell patch-clamp configuration.**(a) Transient and steady state current components of a cell under hyperpolarizing voltage step of −10mV from a holding potential of −60mV for 30ms. Resistance determined from the steady state current was used to evaluate the membrane capacitance obtained from the time constant determined from a bi-exponential fit of the transient current accounting for the pipette leakage. (b) Transient and steady state current components of a cell under depolarizing voltage step of 20mV from a holding potential of −60mV for 30ms. Average capacitance obtained from the hyperpolarizing voltage steps was used to quantify the membrane time constant under depolarizing conditions. A tri-exponential fitting model for the transient depolarizing current including the pre-determined membrane time constant as one of the exponential components would then yield a fitting function that represents the total transient current as a sum of three transient components namely, pipette leakage component, membrane leakage component and the gating current component.

Supporting Figure S12

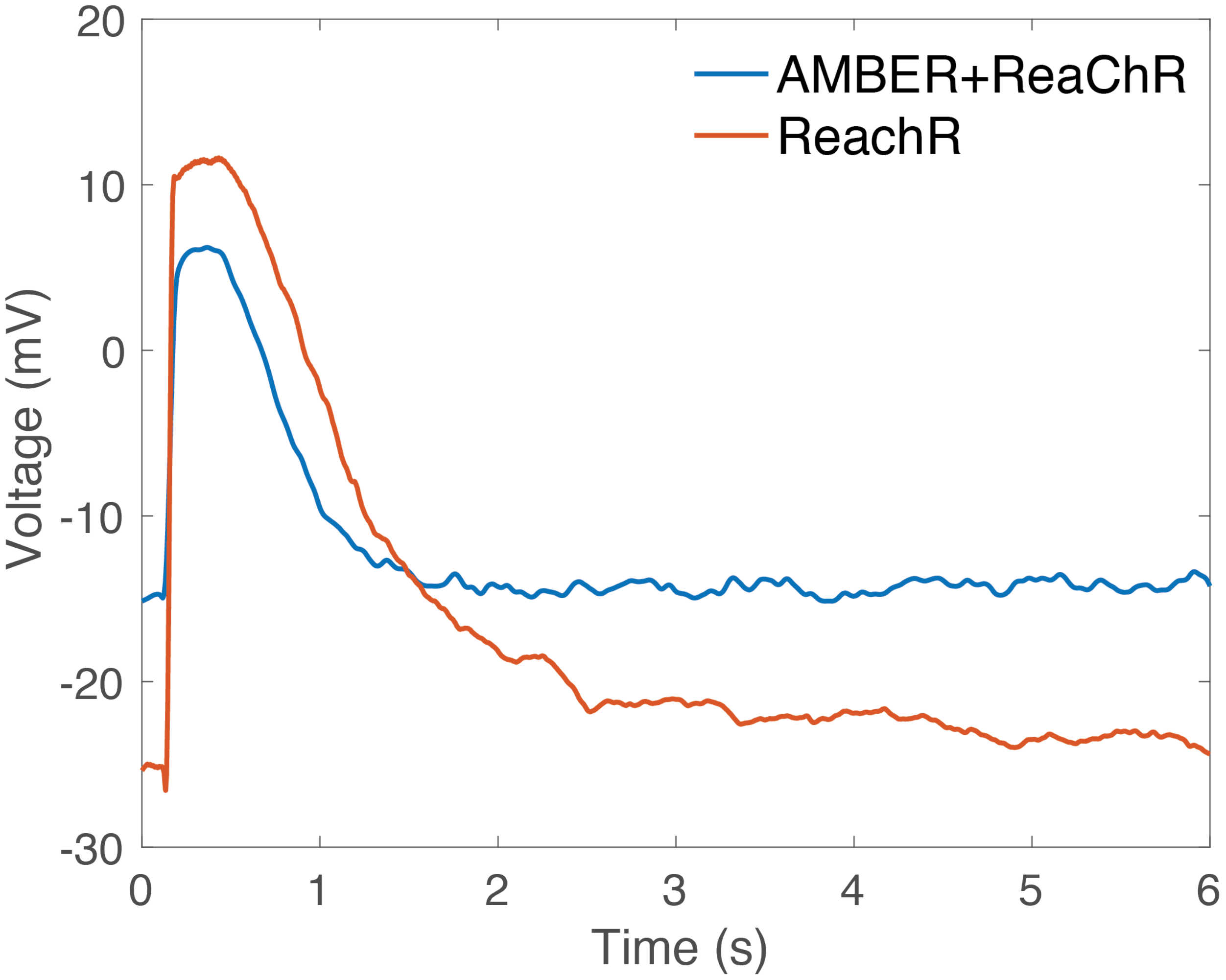

Figure S12: **Representative Light activated voltage transients of HEK293 cells co-expressing AMBER+ReaCHR and ReaCHR only.** Resting potential of a cell co-expressing AMBER+ReaCHR is slightly more positive than cells expressing ReaCHR only

Supporting Figure S13

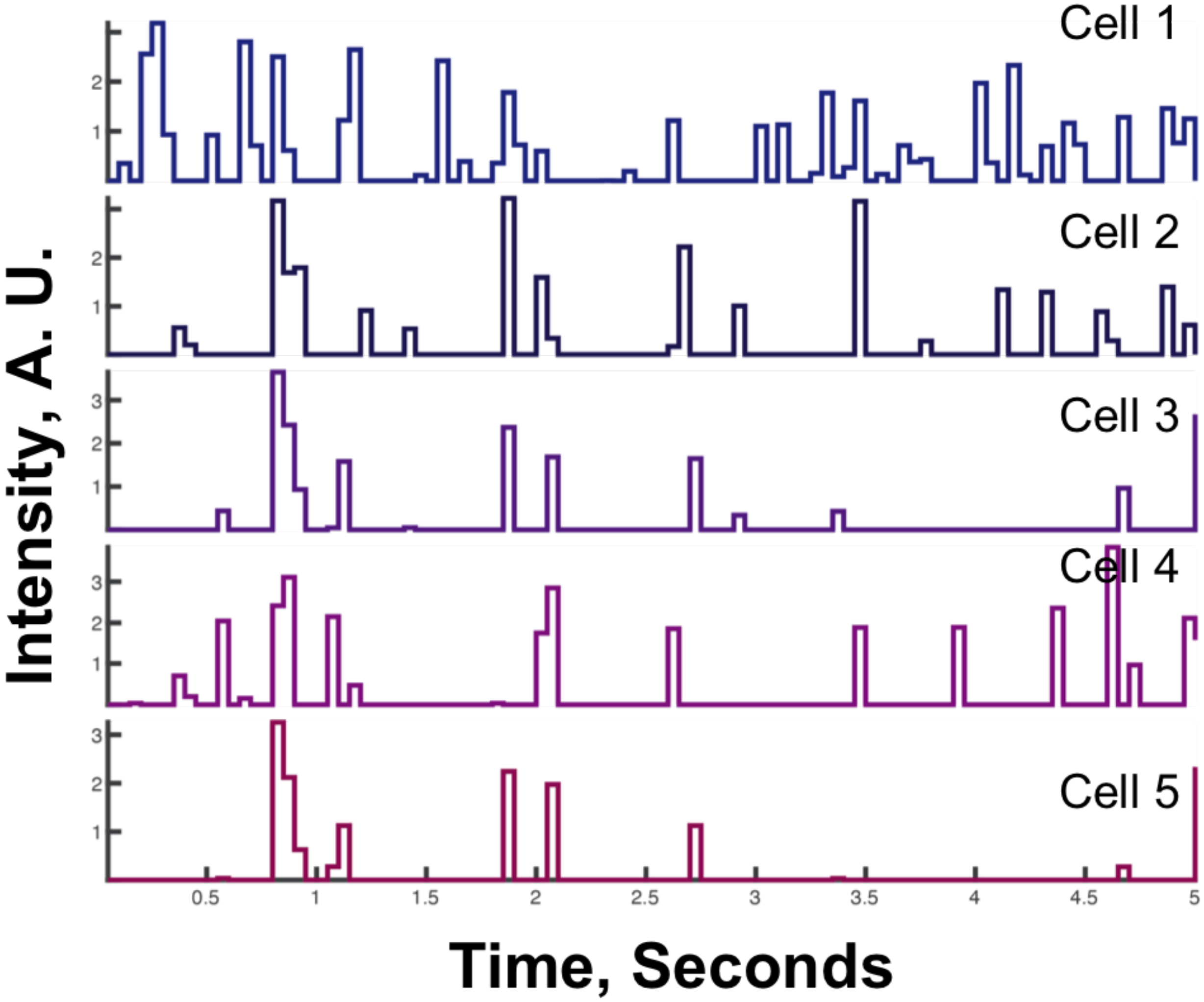

Figure S13: **Single cell bioluminescence transients co-expressing AmBER+ReaCHR after 300ms photoactivation.** An example of AMBER signal transient traces obtained from a population of single isolated cells (n= 8 cells) after photoactivation. A majority of the cells show characteristic exponential decay of the signal (as Cell 1, 2, 3 and 5) after photoactivation. Signal-to-noise ratio of some traces were very low resulting in noisy traces (as Cell 2, 3 and 5).

Supporting Figure S14

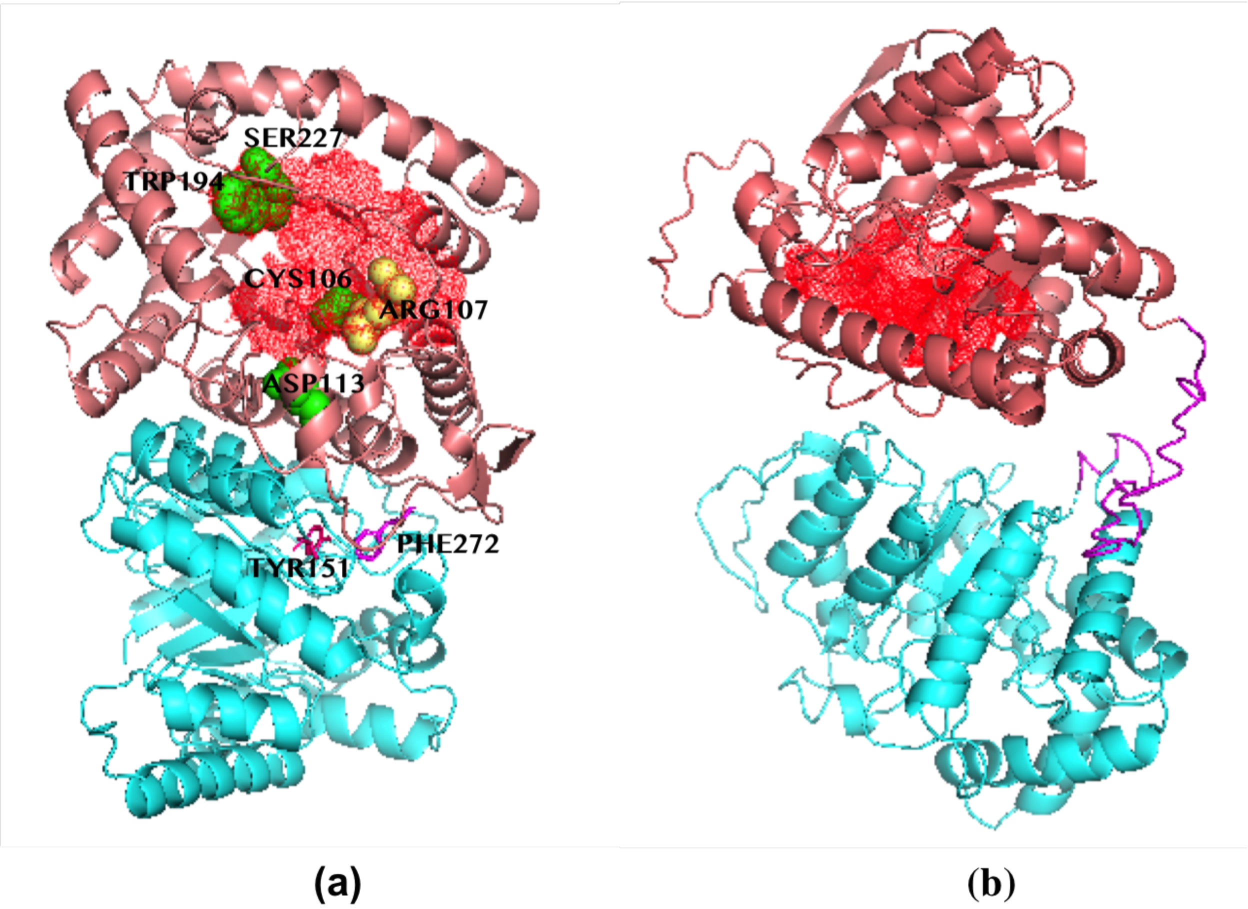

Figure S14: **Geometry of the eluxAB FMN pocket is affected by the association constraint between the subunits.**(a) Crystal structure of vh-luxAB in the FMN unbound state published earlier [3]. Hydrophobic interaction at the interface of the α (pink) and β (cyan) subunits is critical for the FMN binding pocket to maintain its geometry ($[\text{vh-luxAB}]^{\text{ub}}_{\text{SA}} \approx 558.45\text{Å}^2$) . SER227, TRP194, CYS106, and ASP113 are active centre residues (green spheres). CYS106 and ARG107 (yellow spheres) are part of the putative aldehyde binding domain. Contact between αPHE272 and βTYR151 within a distance of ≈ 7.1 Å [3] is achieved due to the interfacial distance constraints as a result of hydrophobic interaction. FMN binding pocket is shown as a meshed surface (red). (b) Predicted structure of the fused eluxAB molecule and its contracted FMN pocket. eluxA (pink), fusion linker (magenta), eluxB (cyan) and its FMN binding pocket (red) are shown. The chosen model ranks first (C-score = -2.66; Estimated TM-score = 0.41 ± 0.14; Estimated RMSD = 14.8 ± 3.6Å) among the top five predicted candidates. Majority of the top ten threading templates used for the prediction were from the chains of the vh-luxAB (PDBID: 3FGC). The solvent accessible surface area of the FMN binding pocket ($[\text{eluxAB}]_{\text{SA}} \approx 345.14\text{Å}^2$) is lesser than $[\text{vh-luxAB}]^{\text{ub}}_{\text{SA}}$ evaluated using the crystal structure.

Supporting Figure S15

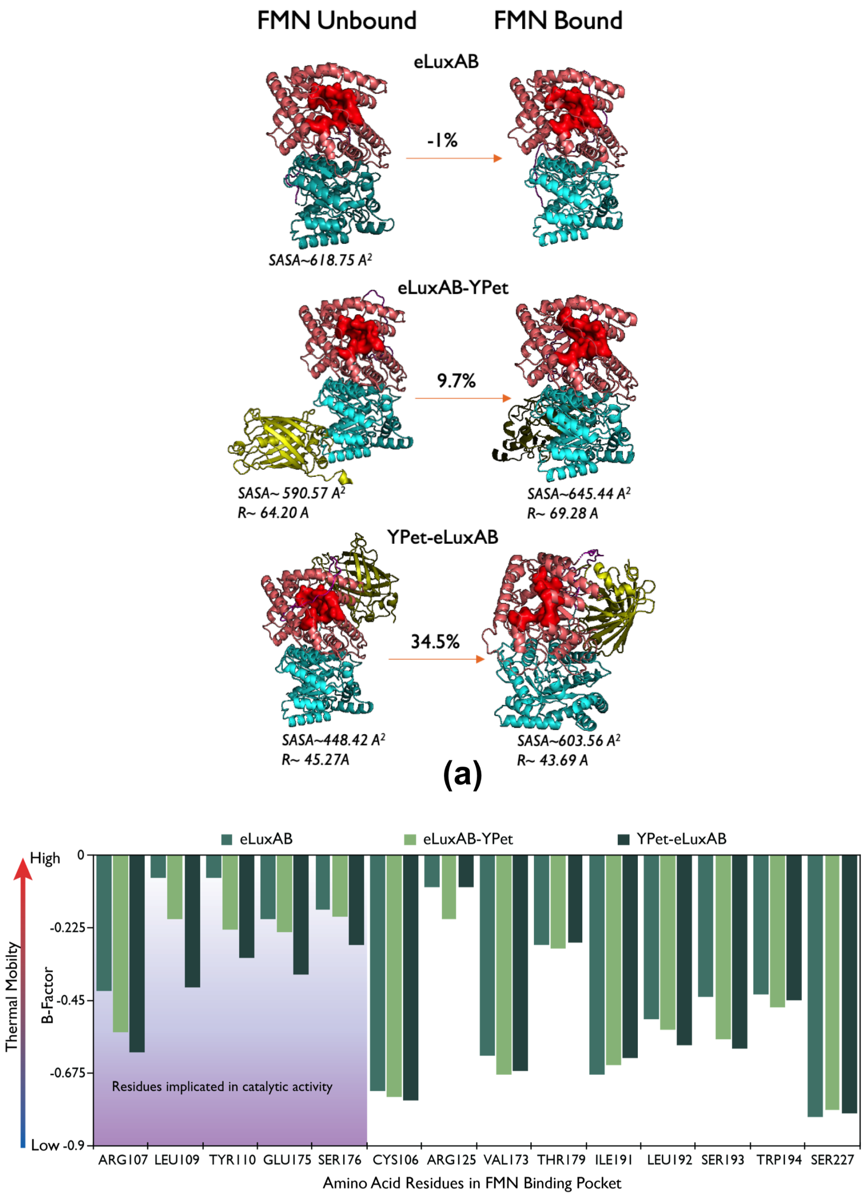

(a)

(b)

Figure S15: **Molecular basis of AMBER function.**Computational structural prediction using I-TASSER for eluxAB, eluxAB-YPet (E-Y) and YPet-eluxAB (Y-E). Difference in the perturbation of FMN binding pocket was quantified by estimating the solvent accessible surface area of the pocket in the unbound/bound states. eluxAB was predicted to undergo the least change ($\approx -1\%$) followed by E-Y($\approx$ 9.7%) and Y-E ($\approx$34.5%). Change in Förster distances was very small for both BRET pairs. (b) Thermal mobility of the FMN binding pocket residues of the predicted models. Significant change in the mobility of ARG107, LEU109, TYR110, GLU175 and SER176 were observed among the predicted models. Y-E FMN pocket has lesser mobility than E-Y pocket at the critical residue locations.

Supporting Figure S16

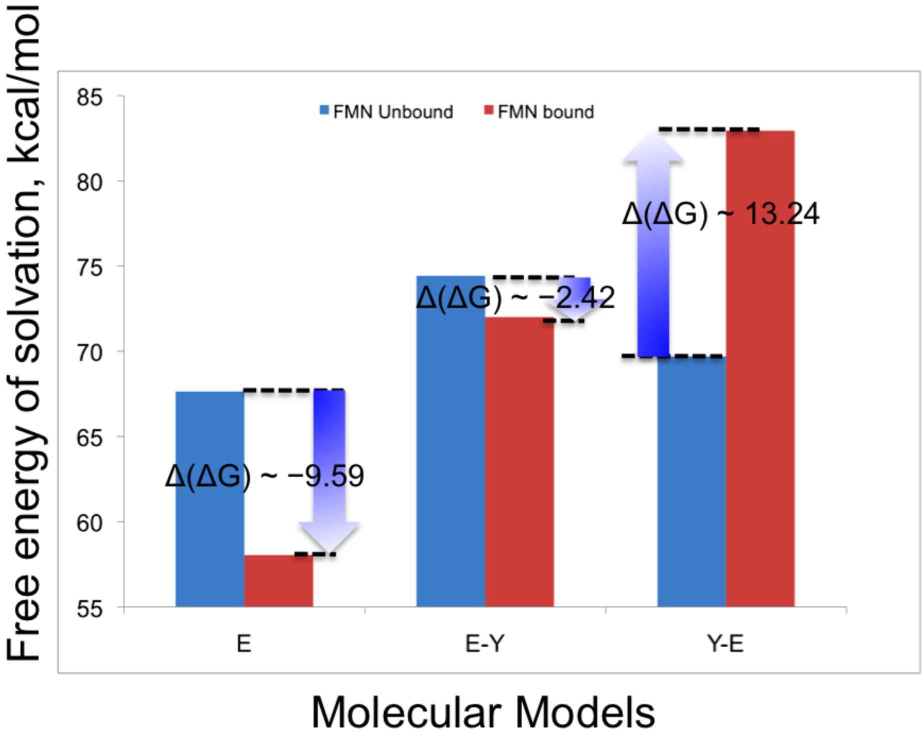

Figure S16: **Free energy barrier associated with the enzymatic activity of the predicted models.** Mean free energy of solvation was estimated using the approach described in [12] for eluxAB, eluxAB-YPet and YPet-eluxAB. eluxAB-YPet was predicted to have a small free energy barrier $(\Delta(\Delta G)) \approx -2.42$ kcal/mol) and is thermodynamically favorable. In contrast, the free energy barrier of YPet-eluxAB is higher $(\Delta(\Delta G) \approx 13.24$ kcal/mol) and is thermodynamically unfavorable. This plot suggests that depolarization-induced conformational change of the VSD can cause the eluxAB-YPet to overcome a relatively smaller activation barrier to turn on the enzymatic light reaction. However, for the case of YPet-eluxAB, this cannot be done efficiently due to a large activation barrier that need to be overcome to complete a thermodynamically unfavourable reaction. For eluxAB, although the reaction is thermodynamically favorable, the free energy difference $(\Delta(\Delta G) \approx -9.59$ kcal/mol) is greater than of eluxAB-YPet.

Supporting Figure S17

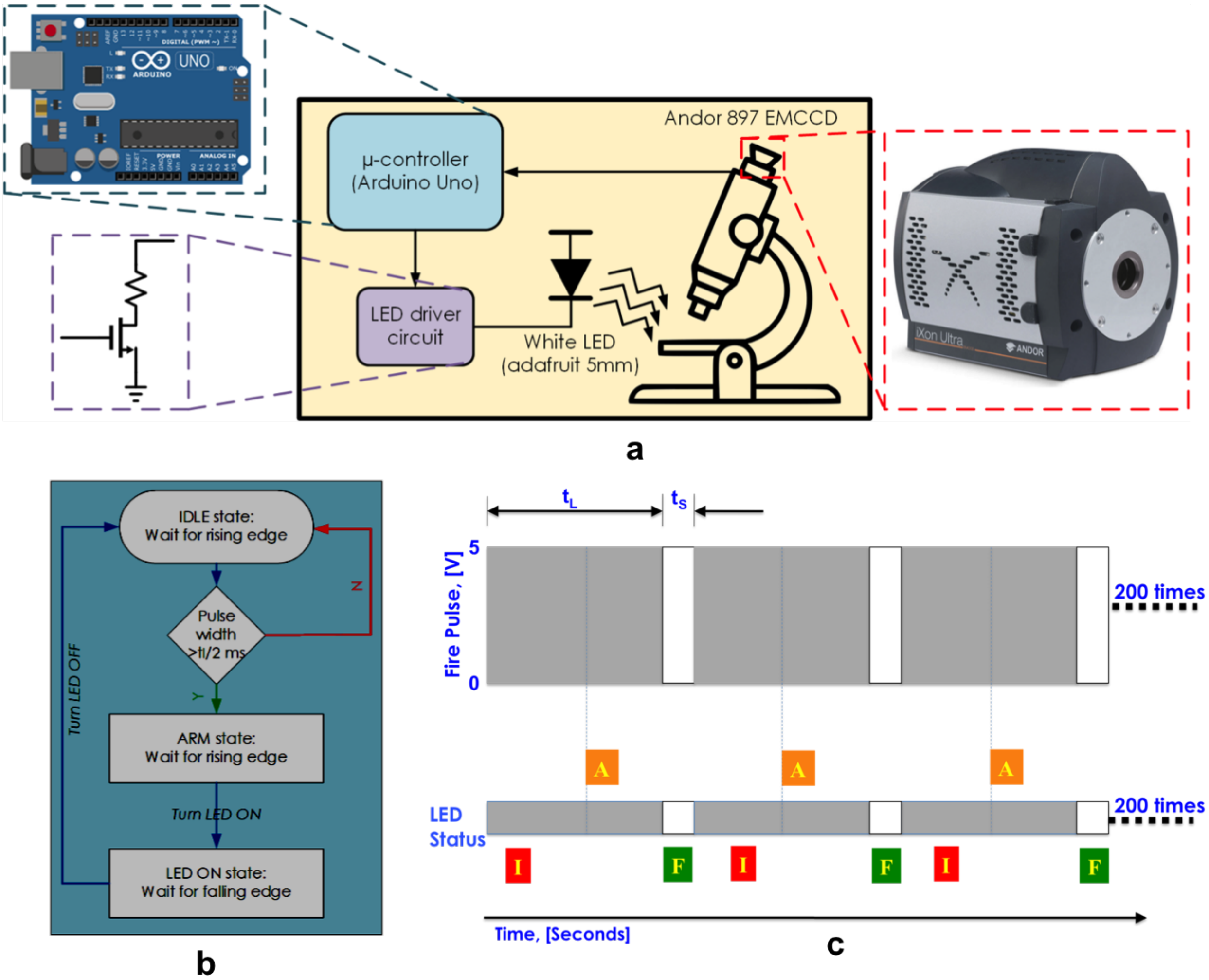

Figure S17: **Custom-built imaging set up to track the worm position during bioluminescent recording.** (a) Schematic of the experimental hardware used for tracking the worm position; (b) Algorithm used for programming the Arduino Uno microcontroller that drives the flash circuit based on the trigger output of the EMCCD camera; (c) Representative LED lighting and camera exposure patterns that allows live tracking during bioluminescent recording. LED status sequentially changes from idle (I) to armed (A) to flash (F). For most recording we used t_L= 0.5-1 sec and t_S= 6 msec respectively.

Supporting Figure S18

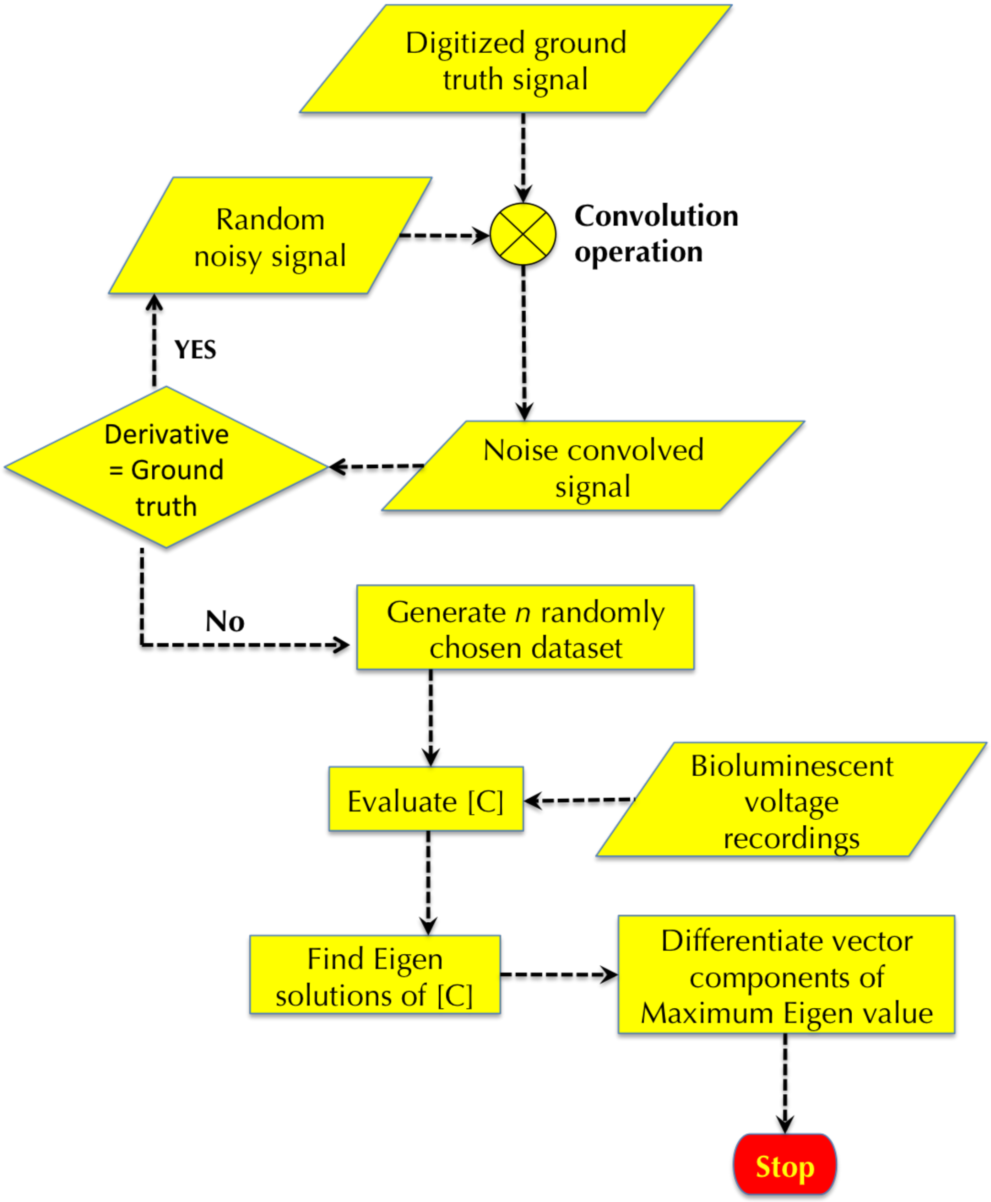

Figure S18: **Algorithm of modified sparse sampling approach.** A flow chart of information transfer, data set generation and processing for the reconstruction of a representative ground truth signal using modified sparse sampling approach.

Supporting Figure S19

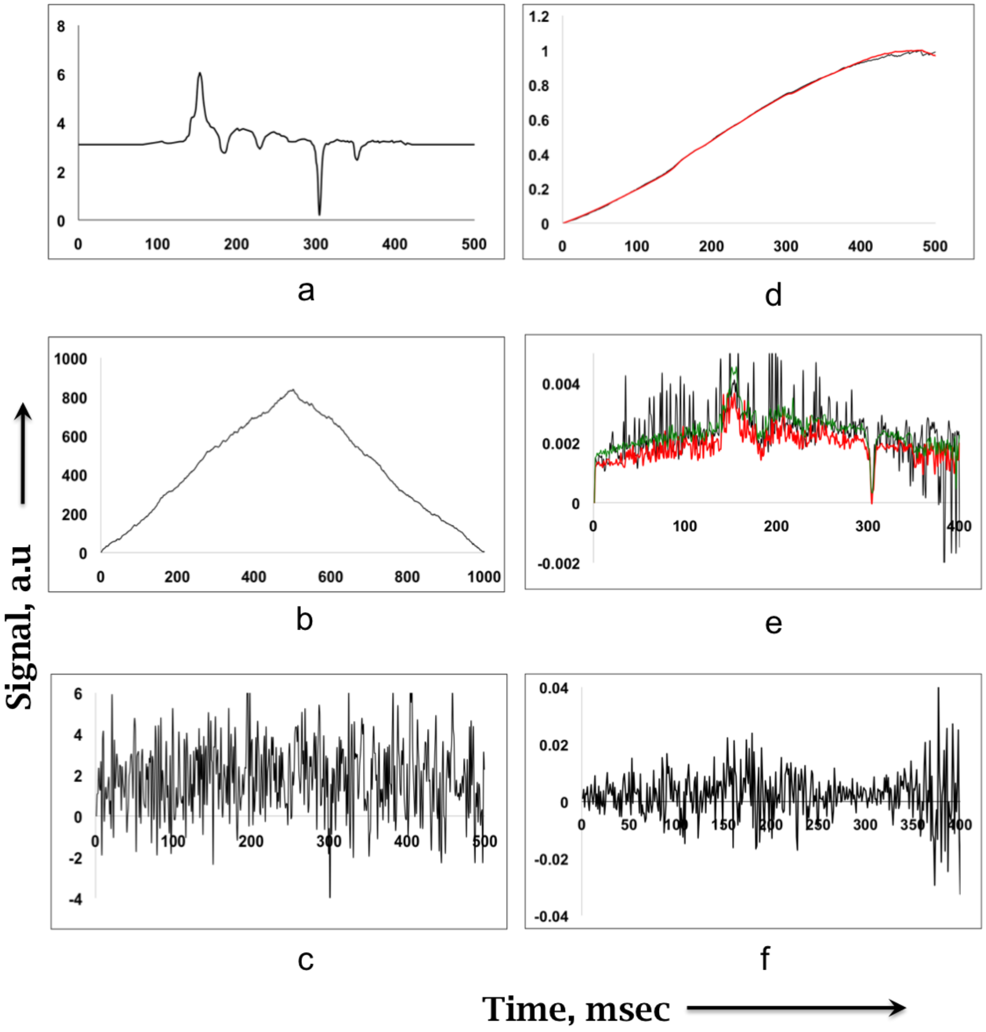

Figure S19: **Reconstruction of the EPG trace applying the modified sparse sampling approach.** (a) A typical EPG trace obtained by digitizing the data published in [9]. (b) EPG trace convolved with a 500ms random noise. (c) Derivative of the noise-convolved EPG trace within 500ms. (d) Eigen vector corresponding to the maximum eigen value representing the integrated ground truth signal for n = 200 (Black) recorded samples and n= 3000 (Red) samples obtained after bootstrap with replacement. (e) Representative ground truth signals for different sample sizes obtained by differentiating the Eigen vector corresponding to the maximum Eigen value; n= 200 (Black), n= 1000 (Red) and n= 3000 (Green). Red and Green traces were obtained by bootstrap sampling with replacement. (f) Representative ground truth using randomly generated time-integrated input gives a completely uncorrelated output.

Supporting Figure S20

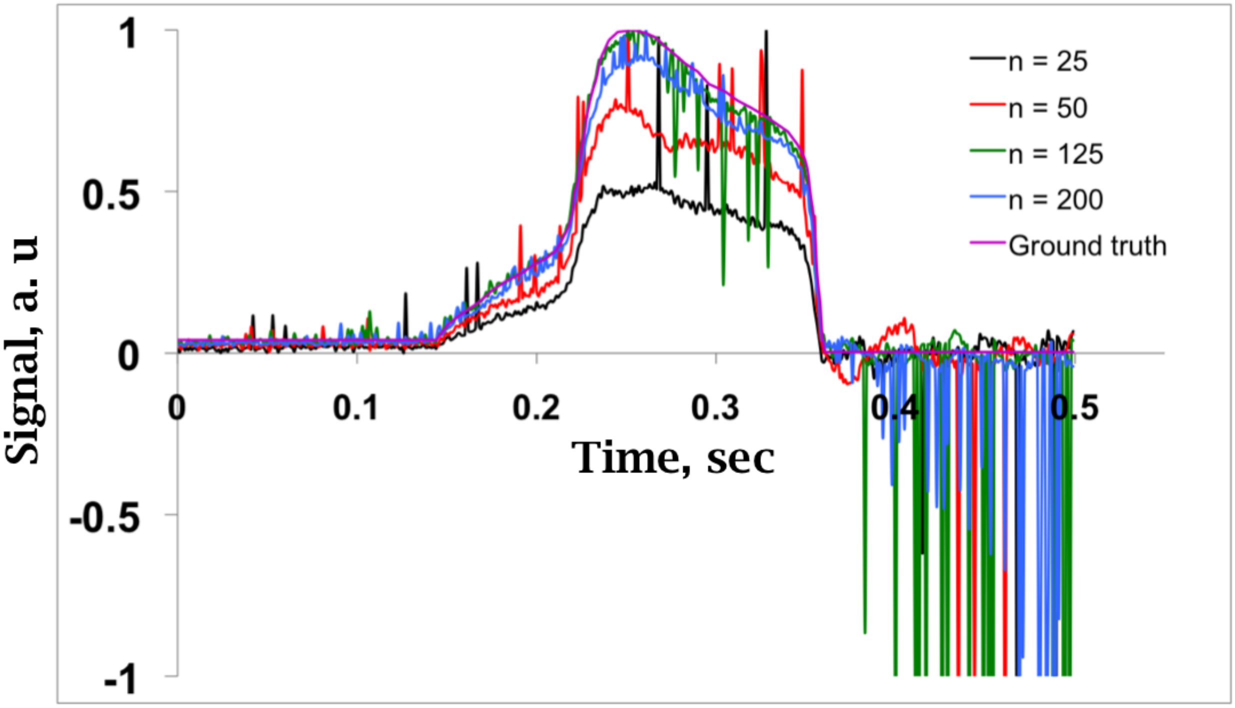

Figure S20: **Reconstruction of the Terminal bulb action potential using modified sparse sampling approach for different sample sizes.** Signal-to-Noise ratio of the reconstructed representative traces improved with increasing sample size, n = 25, 50, 125 and 200. Ground truth data was obtained by digitizing the electrically recorded data published previously [8]

Supporting Figure S21

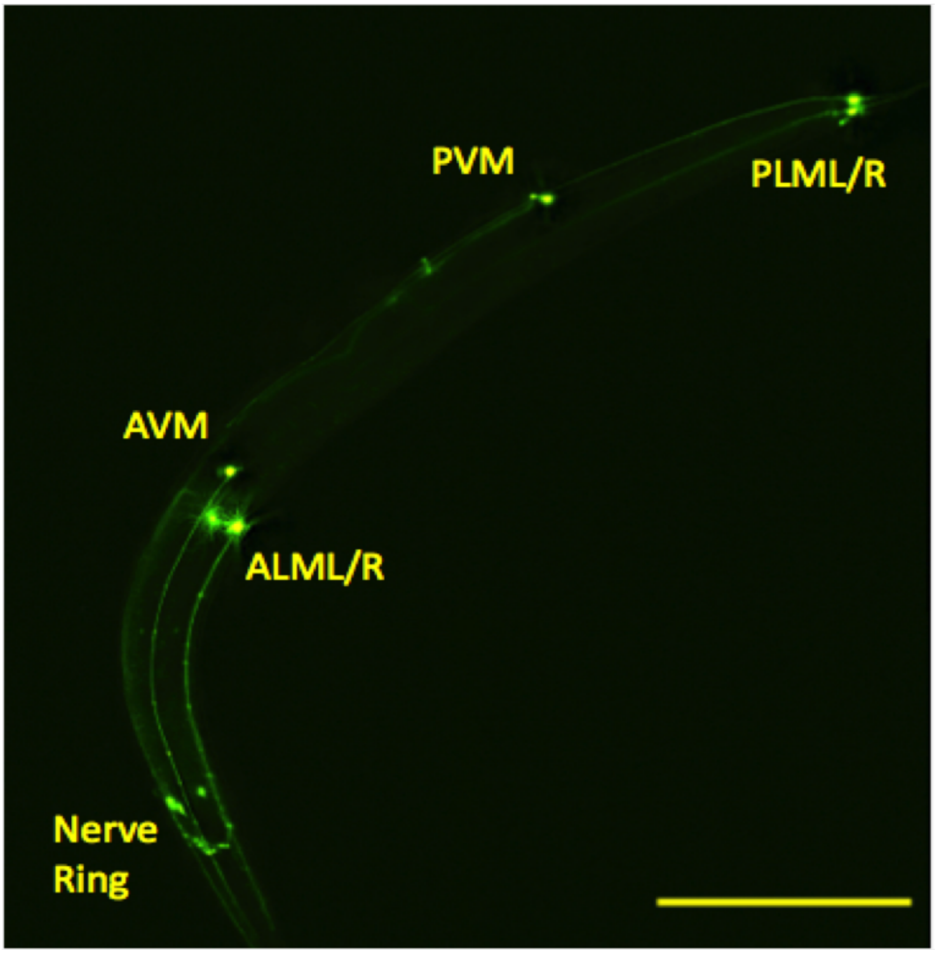

Figure S21: **Mapping C.*elegans* touch neuronal circuit identified previously** Soma of the touch neurons (PLML/R, PVM, AVM, ALML/R, and Nerve Ring) were precisely identified using the fluorescent eGFP driven by the mec-7 promoter. The scale bar length is 250μm.

Supporting Figure S22

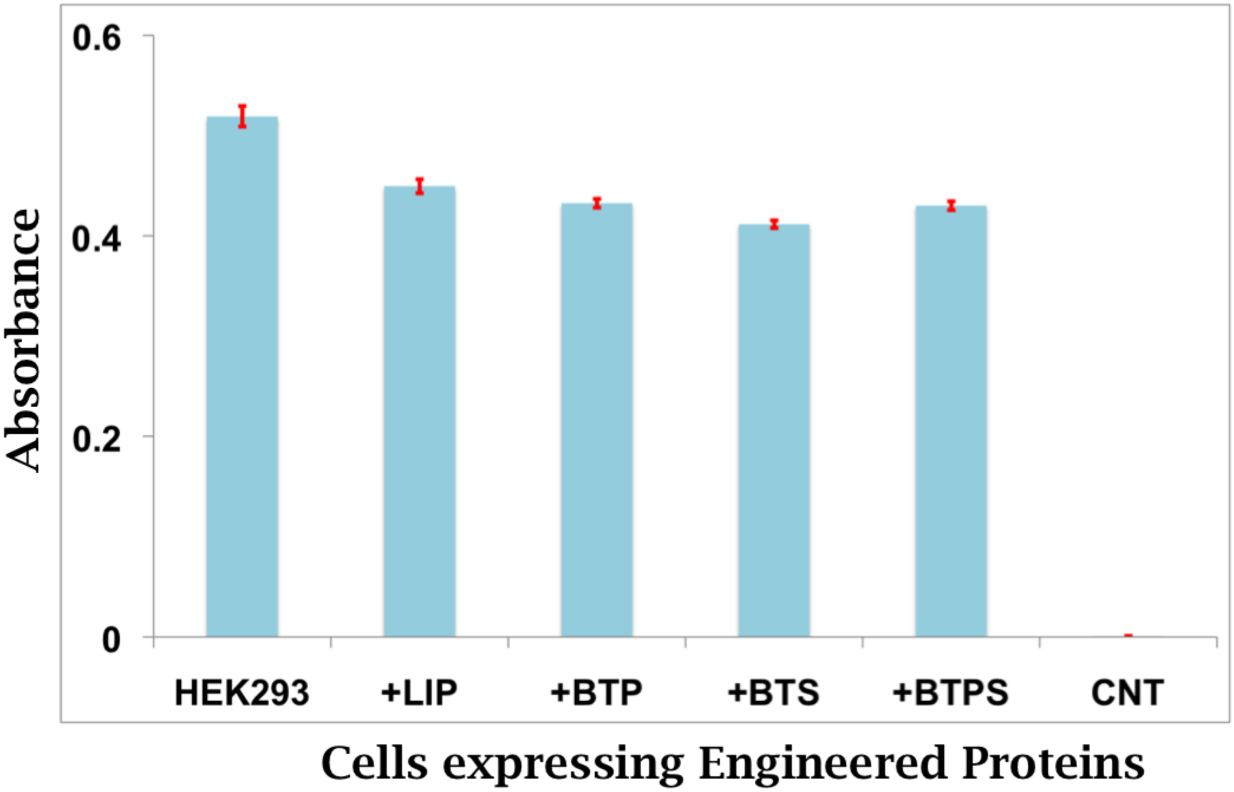

Figure S22: **Viability of HEK293 cells is not significantly compromised due to the expression of AMBER proteins** Absorbance of MTT reagent treated with as grown HEK293 cells (HEK), cells treated with Lipofectamine-2000 transfection reagent (+LIP), cells expressing FV-E-Y (+BTP), luxCDE (+BTS) and AMBER (+BTPS). CNT refers to the absorbance of the untreated MTT reagent (negative control). Reported absorbance values are Mean ± SEM.

Supporting Figure S23

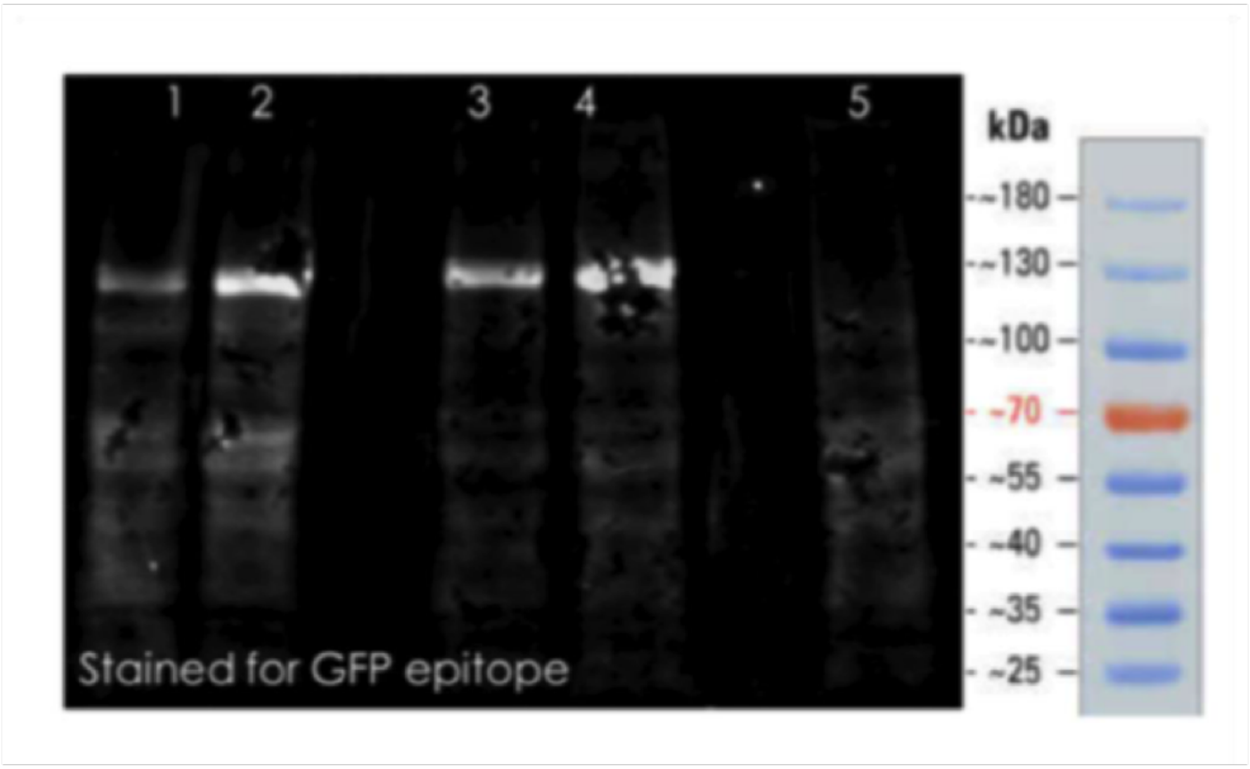

Figure S23: **Comparison of the expression of engineered protein in HEK293 cells using Western blot assay.** YPet is stained using an antibody that targets an epitope conserved across all the GFP variants. VSD-YPet-eluxAB (Lane-1), VSD-YPet-eluxAB+luxCDE (Lane-2), VSD-eluxAB-YPet (Lane-3), VSD-eluxAB YPet+luxCDE (Lane-4), and untransfected HEK293 cells (Lane-5). Lane-1 sample was diluted to half to compare the range of expression levels of all the chosen candidates. Marker lane indicating the molecular weight in KDa is shown on the right side of the blot. The estimated molecular weight ($\approx$ 133 KDa) agrees closely with the predicted average value for 1213 residues assuming a residue molecular weight of $\approx$ 110g/mol.

References

[1] Thomas O. Baldwin, Jon A. Christopher, Frank M. Raushel, James F. Sinclair, Miriam M. Ziegler, Andrew J. Fisher, and Ivan Rayment. Structure of bacterial luciferase. Current Opinion in Structural Biology, 5(6):798–809, 1995.

[2] S. Brenner. The genetics of Caenorhabditis elegans. Genetics, 77(1):71–94, 1974.

[3] Zachary T. Campbell, Andrzej Weichsel, William R. Montfort, and Thomas O. Baldwin. Crystal structure of the bacterial luciferase/flavin complex provides insight into the function of the β subunit. Biochemistry, 48(26):6085–6094, 2009.

[4] Erhu Cao, Julio F. Cordero-Morales, Beiying Liu, Feng Qin, and David Julius. TRPV1 Channels Are Intrinsically Heat Sensitive and Negatively Regulated by Phosphoinositide Lipids. Neuron, 77(4):667–679, 2013.

[5] Tony J. Collins. ImageJ for microscopy. BioTechniques, 43(1 Suppl):25–30, 2007.

[6] Anna Cleta Croce and G. Bottiroli. Autofluorescence spectroscopy and imaging: A tool for biomedical research and diagnosis. European Journal of Histochemistry, 58(4):320–337, 2014.

[7] Boyu Cui, Lifeng Zhang, Yunhong Song, Jinsong Wei, Changfu Li, Tietao Wang, Yao Wang, Tianyong Zhao, and Xihui Shen. Engineering an enhanced, thermostable, monomeric bacterial luciferase gene as a reporter in plant protoplasts. PLoS ONE, 9(10):107885, 2014.

[8] M. Wayne Davis, Richard Fleischhauer, Joseph A. Dent, Rolf H. Joho, and Leon Avery. A mutation in the C. elegans EXP-2 potassium channel that alters feeding behavior. Science, 286(5449):2501–2504, 1999.

[9] James Dillon, Ioannis Andrianakis, Kate Bull, Steve Glautier, Vincent O'Connor, Lindy Holden-Dye, and Christopher James. AutoEPG: Software for the analysis of electrical activity in the microcircuit underpinning feeding behaviour of Caenorhabditis elegans. PLoS ONE, 4(12):8482, 2009.

[10] Dimitar Dimitrov, You He, Hiroki Mutoh, Bradley J. Baker, Lawrence Cohen, Walther Akermann, and Thomas Knöpfel. Engineering and characterization of an enhanced fluorescent protein voltage sensor. PLoS ONE, 2(5):440, 2007.

[11] Arthur D Edelstein, Mark A Tsuchida, Nenad Amodaj, Henry Pinkard, Ronald D Vale, and Nico Stuurman. Advanced methods of microscope control using μManager software. Journal of Biological Methods, 1(2):10, 2014.

[12] David Eisenberg and Andrew D. Mclachlan. Solvation energy in protein folding and binding. Nature, 319(6050):199–203, 1986.

[13] Thomas Evans. Transformation and microinjection. WormBook, 2006.

[14] Andrew J. Fisher, Ivan Rayment, Frank M. Raushel, and Thomas O. Baldwin. Three-Dimensional Structure of Bacterial Luciferase from Vibrio Harveyi at 2.4. Å Resolution. Biochemistry, 34(20):6581–6586, 1995.

[15] Woods Gonzalez and Richard E Woods. Eddins, Digital Image Processing Using MATLAB, volume 11. Prentice Hall, New Jersey, 2004.

[16] Carola Gregor, Klaus C. Gwosch, Steffen J. Sahl, and Stefan W. Hell. Strongly enhanced bacterial bioluminescence with the ilux operon for single-cell imaging. Proceedings of the National Academy of Sciences of the United States of America, 115(5):962–967, 2018.

[17] Oliver Griesbeck, Geoffrey S. Baird, Robert E. Campbell, David A. Zacharias, and Roger Y. Tsien. Reducing the environmental sensitivity of yellow fluorescent protein. Mechanism and applications. Journal of Biological Chemistry, 276(31):29188–29194, 2001.

[18] Negin Azimi Hashemi, Amelie C.F. Bergs, Christina Schüler, Anna Rebecca Scheiwe, Wagner Steuer Costa, Maximilian Bach, Jana F. Liewald, and Alexander Gottschalk. Rhodopsin-based voltage imaging tools for use in muscles and neurons of Caenorhabditis elegans. Proceedings of the National Academy of Sciences of the United States of America, 116(34):17051–17060, 2019.

[19] W Humphrey, A Dalke, and K Schulten. VMD-Visual Molecular Dynamics. J. Molec. Graphics, 14:33–38, 1996.

[20] S Iwano. Single-cell bioluminescence imaging of deep tissue in freely moving animals. Science, 359:935–39,, 2018.

[21] Zahra Karimi, Sajad Falsafi-Zadeh, Hamid Galehdari, and Amir Jalali. Homology modeling and molecular dynamics simulation of odonthubuthus doriae (Od1) scorpion toxin in comparison to the BmK M1. Bioinformation, 8(10):474–478, 2012.

[22] L. Kovarik, A. Stevens, A. Liyu, and N. D. Browning. Implementing an accurate and rapid sparse sampling approach for low-dose atomic resolution STEM imaging. Applied Physics Letters, 109(16):164102, 2016.

[23] T J Lambert. FPbase: A community-editable fluorescent protein database. Nature Methods, 16:227–278, 2019.

[24] Qufei Li, Sherry Wanderling, Marcin Paduch, David Medovoy, Abhishek Singharoy, Ryan Mcgreevy, Carlos A. Villalba-Galea, Raymond E. Hulse, Benoît Roux, Klaus Schulten, Anthony Kossiakoff, and Eduardo Perozo. Structural mechanism of voltage-dependent gating in an isolated voltage-sensing domain. Nature Structural and Molecular Biology, 21(3):244–252, 2014.

[25] Leo Yen-Cheng Lin, Traian Sulea, Rose Szittner, Vladislav Vassilyev, Enrico O. Purisima, and Edward A. Meighen. Modeling of the bacterial luciferase-flavin mononucleotide complex combining flexible docking with structure-activity data. Protein Science, 10(8):1563–1571, 2001.

[26] Omer Mano, Matthew S. Creamer, Catherine A. Matulis, Emilio Salazar-Gatzimas, Juyue Chen, Jacob A. Zavatone-Veth, and Damon A. Clark. Using slow frame rate imaging to extract fast receptive fields. Nature Communications, 10(1):4979, 2019.

[27] Craig Mello and Andrew Fire. DNA Transformation. Methods in Cell Biology, 48(C):451–482, 1995.

[28] Tim Mosmann. Rapid colorimetric assay for cellular growth and survival: Application to proliferation and cytotoxicity assays. Journal of Immunological Methods, 65(1-2):55–63, 1983.

[29] Annalee W. Nguyen and Patrick S. Daugherty. Evolutionary optimization of fluorescent proteins for intracellular FRET. Nature Biotechnology, 23(3):355–360, 2005.

[30] Olof Olsson, Alan Escher, Göran Sandberg, Jeff Schell, Csaba Koncz, and Aladar A. Szalay. Engineering of monomeric bacterial luciferases by fusion of luxA and luxB genes in Vibrio harveyi. Gene, 81(2):335–347, 1989.

[31] A Rohatgi. WebplotDigitizer: Version 4.4.

[32] C. Savage, M. Hamelin, J. G. Culotti, A. Coulson, D. G. Albertson, and M. Chalfie. mec-7 is a beta-tubulin gene required for the production of 15-protofilament microtubules in Caenorhabditis elegans. Genes & development, 3(6):870–881, 1989.

[33] Caroline A. Schneider, Wayne S. Rasband, and Kevin W. Eliceiri. NIH Image to ImageJ: 25 years of image analysis. Nature Methods, 9(7):671–675, 2012.

[34] Monika Scholz, Aaron R. Dinner, Erel Levine, and David Biron. Stochastic feeding dynamics arise from the need for information and energy. Proceedings of the National Academy of Sciences of the United States of America, 114(35):9261–9266, 2017.

[35] Odelia Schwartz, Jonathan W. Pillow, Nicole C. Rust, and Eero P. Simoncelli. Spike-triggered neural characterization. Journal of Vision, 6(4):484–507, 2006.

[36] C. E. Shannon. A Mathematical Theory of Communication. Bell System Technical Journal, 27(3):379–423, 1948.

[37] Andrea L. Szymczak, Creg J. Workman, Yao Wang, Kate M. Vignali, Smaroula Dilioglou, Elio F. Vanin, and Dario A.A. Vignali. Correction of multi-gene deficiency in vivo using a single 'self-cleaving' 2A peptide-based retroviral vector. Nature Biotechnology, 22(5):589–594, 2004.

[38] Yang Zhang. I-TASSER server for protein 3D structure prediction. BMC Bioinformatics, 9:40, 2008.

[39] Yubin Zhou, Prasanna Srinivasan, Shiva Razavi, Sam Seymour, Paul Meraner, Aparna Gudlur, Peter B. Stathopulos, Mitsuhiko Ikura, Anjana Rao, and Patrick G. Hogan. Initial activation of STIM1, the regulator of store-operated calcium entry. Nature Structural and Molecular Biology, 20(8):973–981, 2013.